

# Comparing 1-year GUMICS–4 simulations of the Terrestrial Magnetosphere with Cluster Measurements

G. Facskó<sup>1,2,3\*</sup>, D. G. Sibeck<sup>2</sup>, I. Honkonen<sup>4</sup>, L. Degener<sup>4†</sup>, P. Peitso<sup>5‡</sup>,  
E. I. Tanskanen<sup>5</sup>, C. R. Anekallu<sup>6</sup>, J. Kalmár<sup>1</sup>, J. Bór<sup>1</sup>, G. Farinas Perez<sup>2,3§</sup>,  
S. Szalai<sup>1</sup>, Á. Kis<sup>1</sup>, V. Wesztergom<sup>1</sup>

<sup>1</sup>HAS Research Centre for Astronomy and Earth Sciences, Sopron, Hungary

<sup>2</sup>NASA Goddard Space Flight Center, Greenbelt, Maryland, USA

<sup>3</sup>the Catholic University of America, Washington DC, USA

<sup>4</sup>Finnish Meteorological Institute, Helsinki, Finland

<sup>5</sup>Aalto University, School of Electrical Engineering, Espoo, Finland

<sup>6</sup>UCL Department of Space & Climate Physics, Mullard Space Science Laboratory, Dorking, UK

## Key Points:

- The GUMICS–4 provides realistic ion plasma moments and magnetic field in the solar wind and the outer magnetosheath.
- The code can provide the realistic location of the bow shock.
- An inner magnetosphere model should add to the code to increase the accuracy of the simulation.

\*Now at Rhea System GmbH, TIZ Building, Robert Bosch Str. 7, 64293 Darmstadt, Germany

†Now private individual, Hannover, Germany

‡Now at Aurora Propulsion Technologies, Espoo, Finland

§Now at University of Miami, Electrical and Computer Engineering Department, Miami, Florida, USA

Corresponding author: Gábor Facskó, [gabor.i.facsko@gmail.com](mailto:gabor.i.facsko@gmail.com)

18      **Abstract**

19      Previously 1-year global magnetohydrodynamics simulation was made using the GUMICS–4  
 20     code and the OMNI 1-min resolution solar wind data from January 29, 2002 to Febru-  
 21     ary 2, 2003 as input. Along the orbit of the Cluster SC3 reference spacecraft the sim-  
 22     ulation data was saved. We compare the saved parameters to the Cluster SC3 measure-  
 23     ments. We use the magnetic field Z component, the solar wind velocity X component  
 24     and the solar wind density of the Cluster magnetometer, ion plasma and spacecraft po-  
 25     tential measurements geocentric solar ecliptic reference frame. We select intervals in the  
 26     solar wind, the magnetosheath and the magnetosphere where the instruments above pro-  
 27     vided good quality data and the spacecraft and the simulation are in the same region.  
 28     We determine the location of the bow shock, the magnetopause and the neutral sheet  
 29     in the spacecraft measurements and compare their position in the observation and sim-  
 30     ulations.

31      The GUMICS–4 provides quite good results in the solar wind. Its accuracy is sig-  
 32     nificantly worse in the magnetosheath. The simulation results are not realistic in the mag-  
 33     netosphere. The bow shock location is predicted well however the magnetopause loca-  
 34     tion is less accurate. The neutral sheet positions are located quite well thank to the spe-  
 35     cial solar wind conditions. The reason of these inaccuracies is the missing inner magne-  
 36     tosphere model and the obsolete algorithms applied in the code.

37      **1 Introduction**

38      The most cost-effective way to study the interaction of the solar wind and the plan-  
 39     etary magnetospheres (or predict the conditions of the near-Earth space) is using a global  
 40     magnetohydrodynamics (MHD) code. Robust parallelized, effective, verified and vali-  
 41     dated codes were developed, are used and applied to forecast the cosmic environment  
 42     of the Earth; such as the Lyon-Fedder-Mobarry, LFM [Lyon *et al.*, 2004] code, the Open  
 43     Geospace General Circulation Model, OpenGGCM [Raeder *et al.*, 2008], the Block-Adaptive-  
 44     Tree-Solarwind-Roe-Upwind-Scheme, BATS-R-US [Powell *et al.*, 1999; Tóth *et al.*, 2012].  
 45     In Europe only three global MHD codes were developed: the Grand Unified Magnetosphere–  
 46     Ionosphere Coupling Simulation [GUMICS–4; Janhunen *et al.*, 2012], the COOLFluiD  
 47     [Lani *et al.*, 2012] and the GORGON 3D magnetohydrodynamic code. The COOLFluiD  
 48     is a general-purpose plasma simulation tool. The Gorgon code was developed for study-  
 49     ing high energy, collisional plasma interactions and has been adapted to simulate plan-

etary magnetospheres and their interaction with the solar wind [Mejnertsen *et al.*, 2016, 2018]. The GUMICS–4 was developed to study the solar wind-terrestrial magnetosphere interaction and its paralel version has not been available for the scientific community (see Section 2.1). These codes are available at the Community Coordinated Modelling Center (CCMC; <http://ccmc.gsfc.nasa.gov/>) hosted by the NASA Goddard Space Flight Center (GSFC). The comparison of the simulation results to spacecraft and ground-based measurements is necessary to understand the abilities and features of the developed tools. The statistical study using long term global MHD runs for validation and verification of the codes seems to be a good and fruitful method. However, providing long simulations is costly and time consuming hence only a few study had done previously using much shorter simulations than a year.

*Guild et al.* [2008a,b] launched two months of LFM run and compared the plasma sheets properties in the simulated tail to the statistical properties of six years Geotail magnetic field and plasma observations [Kokubun *et al.*, 1994; Mukai *et al.*, 1994]. The LFM successfully reproduced the global features of the global plasma sheet in statistical sense. However, there were some differences. The sheet was too cold, too dense and the bulk flow was faster than the observed plasma sheet. The LFM overestimated the ionospheric transpolar potential. The transpolar potential correlated with the speed of the plasma sheet flows. The equatorial maps of density, thermal pressure, thermal energy and velocity were compared. The LFM overestimated the plasma sheet density close to the Earth and underestimated the temperature by a factor of  $\sim 3$ . The LFM overestimated the global average flow speed by a factor of  $\sim 2$ . The LFM reproduced many of the climatological features of the Geotail data set. The low-resolution model underestimated the occurrence of the fast earthward and tailward flows. Increasing the simulation resolution resulted the development of fast, busty flows. These flows contributed the statistics and brought closer the simulations to the observations.

*Zhang et al.* [2011] launched two months long LFM simulation to study the statistics of magnetosphere-ionosphere (MI) coupling. The LFM simulation was also used in the previous study of *Guild et al.* [2008a]. The polar cap potential and the field aligned currents (FAC), the downward Poynting flux and the vorticity of the ionospheric convection were compared with observed statistical averages and the Weimer05 empirical model [Weimer, 2005]. The comparisons showed that the LFM model produced quite accurate average distributions of the Region 1 (R1) and Region 2 (R2) currents. The iono-

spheric Region 2 currents in the MHD simulation seemed to be originated from the diamagnetic ring current. The average LFM Region 1 and 2 currents were smaller compared with the values from the Weimer05 model. The average CPCP was higher in the LFM simulation than the measurements of the SuperDARN and the Weimer05 model. The average convention pattern was quite symmetric in the LFM simulation against the SuperDARN measurements and the Weimer05 model. The SuperDARN measurements and the Weimer05 model had dawn-dusk asymmetry. In the LFM, model more Poynting flux flowed into the polar region ionosphere than in the Weimer05 model. It was the consequence of the larger CPCP in the LFM simulation. The larger CPCP allowed higher electric field in the polar region. The statistical dependence of the high-latitude convection patterns on Interplanetary Magnetic Field (IMF) clock angle was similar to the SuperDARN measurements [Sofko *et al.*, 1995] and the Weimer05 model. The average ionospheric field-aligned vorticity showed good agreement on the dayside. However, the LFM model gave larger nightside vorticity than SuperDARN measurements because the Pedersen conductance on the night side ionosphere was too low.

*Wiltberger et al.* [2017] studied the structure of the high latitude field-aligned current patterns using three resolutions of the LFM global MHD code and the Weimer05 empirical model [Weimer, 2005]. The studied period was a month long and contained two high-speed streams. Generally, the patterns agreed well with results obtained from the Weimer05 computing. As the resolution of the simulations increased, the currents became more intense and narrow. The ratio of the Region 1 (R1), the Region 2 (R2) currents and the R1/R2 ratio increased when the simulation resolution increases. However, both the R1 and R2 currents were smaller than the predictions of the Weimer05 model. This effect led better agreement of the LFM simulation results to the Weimer 2005 model results. The CPCP pattern became concentrated in higher latitudes because of the stronger R2 currents. The relationship of the CPCP and the R1 looked evident at higher resolution of the simulation. The LFM simulation could have reproduced the statistical features of the field aligned current (FAC) patterns.

*Hajducek et al.* [2017] simulated a month of January 2005 using the Space Weather Modelling Framework [SWMF; Tóth *et al.*, 2005] and the OMNI solar wind data as input. The simulations were done with and without inner magnetosphere model and using two different grid resolutions. The model was very good in predicting the currents circling the Earth around the dipole axis [SYM-H; <http://wdc.kugi.kyoto-u.ac.jp/aeasy/asym.pdf>;

*Iyemori*, 1990]. The  $K_p$  index (that measures the general magnetospheric convention and the auroral currents [Bartels *et al.*, 1939; Rostoker, 1972; Thomsen, 2004]) was predicted well during storms however the index was over predicted during quiet time periods. The AL index (that describe the westward electro jet on the surface magnetic field introduced by Davis and Sugiura [1966]) was predicted reasonably well in average however the model reached the highest negative AL value less often than the observations because the model captured poorly the structure of the auroral zone currents. The overpredicting of  $K_p$  index during quiet times might have had the same reason because that index was also sensitive for the auroral zone dynamics. The SWMF usually over predicted the CPCP. These results were not sensitive to grid resolutions. Except that the AL index reached more often the highest negative value when the grid resolution was higher. Switching off of the inner magnetosphere model had dramatic effect for the accuracy of all quantities mentioned above, except the CPCP.

In this paper the Cluster SC3 measurements are compared directly to a previously made 1-year long GUMICS–4 simulation in the solar wind, magnetosheath and the magnetosphere along the Cluster SC3 orbit saved from the simulation results and measured by the spacecraft [Facskó *et al.*, 2016]. Three parameters ( $B_z$ ,  $V_X$  and  $n$ ) were studied and the location of the bow shock, magnetopause and the neutral sheet. The structure of this paper is as follows. Section 2 describes the GUMICS–4 code, the 1-year simulation and the instruments. Section 3 gives comparisons between the simulations and observations. Results of the comparison are discussed in Section 4. Finally, Section 5 contains the conclusions.

## 2 The GUMICS–4 products and Cluster measurements

Here we use two types of very different and difficult time series. The first type is derived from previously made 1-year GUMICS–4 simulation [Facskó *et al.*, 2016]. The second type was measured by the magnetometer, ion plasma and electric field instruments of the Cluster reference spacecraft.

### 2.1 The GUMICS–4 code

The GUMICS–4 has two coupled simulation domains, the magnetospheric domain outside of  $3.7 R_E$  radius around the Earth and a coupled ionosphere module containing

a 3D electron density model if the ionosphere. The GUMICS–4 is not parallel code however the code was extensively used for studying the energy propagation processes from the solar wind to the magnetosphere through the magnetopause and other features [Jan-hunen *et al.*, 2012, see the references therein]. The code had also been applied for study the forced reconnection in the tail [Vörös *et al.*, 2014]. Recently a few hundred of synthetic two hours duration GUMICS–4 simulations was made to compare the simulation results to empirical formulas [Gordeev *et al.*, 2013]. The agreement was quite good however; the diameter of the magnetopause deviated significantly in the simulation and the observations in the tail. The tail of the GUMICS–4 was smaller than spacecraft observed and measured. 1-year long simulation was made using the GUMICS–4 code [Facskó *et al.*, 2016]. Juusola *et al.* [2014] compared the ionospheric currents, fields and the cross polar cap potential (CPCP) in the simulation versus Super Dual Auroral Radar Network (SuperDARN) radars [Greenwald *et al.*, 1995] and CHAMP spacecraft [Reigber *et al.*, 2002] field aligned currents (FAC) measurements [Juusola *et al.*, 2007; Ritter *et al.*, 2004]. The agreement was good the seasonal variation of the CPCP however the FAC and other currents could not be reproduced properly. The possible reason of this bad agreement could be the leak of the inner magnetosphere model. This statement is supported by the result of Haiduček *et al.* [2017]. Haiduček *et al.* simulated only a month using different spatial resolution and to test the codes switched off the inner magnetosphere model of the SWMF for a special run. This run without inner magnetosphere model resulted that only the CPCP parameter of the simulation agreed quite well with the measurement. This fact explained why was so good the agreement between the Cluster SC3 and the GUMICS–4 simulations and gave sense to provide the studies of Lakka *et al.* [2018a,b] based on the CPCP in GUMICS–4 simulations. Kallio and Facskó [2015] determined the solar wind parameters along the Moon orbit using the results of the Facskó *et al.* [2016]’s global MHD simulations. The solar wind parameters differed significantly in the geotail that should have been considered in future studies of the interaction of the solar wind and the lunar orbit. Facskó *et al.* [2016] determined the footprint the Cluster SC3 using the 1-year simulation and the Tsyganenko T96 empirical model [Tsyganenko, 1995]. The code seemed to be react slower for the dynamic changes of the solar wind pressure than the empirical model. The agreement of the footprint is better in the Northern Hemisphere. The GUMICS–4 tail looked shorter in the simulations than the observations. Finally, the Y component of the interplanetary magnetic field twisted the simulated tail hence the agree-

179 ment of the empirical and computational footprints was worse at such solar wind con-  
 180 ditions.

181 A workpackage of the European Cluster Assimilation Technology (ECLAT) project  
 182 ([https://cordis.europa.eu/result/rcn/165813\\_en.html](https://cordis.europa.eu/result/rcn/165813_en.html); <http://www.eclat-project.eu/>) was  
 183 the creation and analysis of 1-year global MHD simulation using the OMNI solar wind  
 184 data from January 29, 2002 to February 2, 2003 as input of the GUMICS-4 code [Fazekas  
 185 et al., 2016]. The GUMICS-4 was a single core system [Janhunen et al., 2012] hence the  
 186 1-year simulation was made in 1860 independent runs. This interval covered 155 Clus-  
 187 ter SC3 orbits and each orbit lasted 57 hours. The supercomputer had 12 CPUs on each  
 188 node hence the 57 hours were divided into 4.7 hours simulation time with one hour ini-  
 189 tialisation period. Each sub-intervals used its own average Geocentric Solar Ecliptic (GSE)  
 190 IMF magnetic field X component  $B_x$  component and dipole tilt angle. All data gaps of  
 191 the input file were filled using interpolation. If the data gap of the input file was at the  
 192 beginning (or the end) interval the first (or last) good data of the input file was used to  
 193 fill the gap. The initialisation of each simulations was made using constant values. These  
 194 values were the first valid data of the input file repeated 60 times (60 minutes) in the  
 195 input file of the sub-interval. The simulation results were saved in every five minutes.  
 196 Various simulation parameters, for example, the density, particle density, temperature,  
 197 magnetic field, solar wind velocity (29 different quantities) were saved from the simu-  
 198 lation results along the Cluster reference spacecraft in the GSE coordinates. In this pa-  
 199 per these parameters, namely the  $B_z$  magnetic field GSE Z component, the solar wind  
 200 velocity GSE X component ( $V_x$ ) and the solar wind density  $n$  are compared to the Clus-  
 201 ter SC3 measurement. These parameters are selected because the  $B_z$  controls the mag-  
 202 netosphere, the  $V_x$  is the main solar wind velocity component and the  $n$  is the ion plasma  
 203 momentum that is the easiest to calculate; furthermore more instruments could deter-  
 204 mine it (see Section 2.2).

## 205 2.2 The Cluster SC3 measurements

206 The Cluster-II spacecraft of the European Space Agency (ESA) were launched in  
 207 2000 and study the geospace since then [Cattaneo et al., 1997; Escoubet et al., 2001]. Its  
 208 four spacecraft form a tetrahedron however here we use only the measurements of the  
 209 reference spacecraft, the Cluster SC3. The spacecraft were stabilised by rotation and its  
 210 period is  $\sim 4$  s. Hence, the temporal resolution of the plasma instruments were consid-

ered 4 s and we use 4 s averaged magnetic field data. The real resolution of the Cluster FluxGate Magnetometer (FGM) magnetic field instrument was 27 Hz [Balogh *et al.*, 1997, 2001]. The ion plasma data was provided by the Cluster Ion Spectrometry (CIS) Hot Ion Analyser (HIA) sub-instrument [Reme *et al.*, 1997; Rème *et al.*, 2001]. The CIS HIA instrument is calibrated using the Waves of HIgh frequency Sounder for Probing the Electron density by Relaxation (WHISPER) wave instrument onboard Cluster [Décréau *et al.*, 2001; Trotignon *et al.*, 2010; Blagau *et al.*, 2013, 2014]. These calibrations might have appeared as sudden non-physical jumps in the CIS HIA data. The CIS HIA had different modes to measure in the solar wind and the magnetosphere. When the instrument switched from a mode to another mode it appeared as a non-physical jump in the measured data too. These features had influence for the accuracy of the data analysis.

We protect our results from these non-physical jumps described previously using a density determination based on different principles. We use the spacecraft potential of the Electric Field and Wave Experiment [EFW ; Gustafsson *et al.*, 1997, 2001] to determine the electron density. This quantity can be calculated using the empirical density formula

$$n_{EFW} = 200(V_{sc})^{-1.85}, \quad (1)$$

where  $n_{EFW}$  is the calculated density and  $V_{sc}$  is the Cluster EFW spacecraft potential [Trotignon *et al.*, 2010, 2011]. The EFW and the WHISPER were used for the calibration of the CIS HIA and the Plasma Electron and Current Experiment [PEACE; Johnstone *et al.*, 1997; Fazakerley *et al.*, 2010a,b]. Both instruments were still working onboard all Cluster spacecraft. Their stable operation reduced the number of data gaps; furthermore made easier the data analysis.

### 3 Comparison of measurements to simulation

The saved parameters from the GUMICS–4 simulations and the Cluster SC3 magnetic field, solar wind velocity and density measurements are compared in the solar wind, magnetosheath and magnetosphere using cross correlation calculation. The resolution of the simulated Cluster orbit data is mostly five minutes because the simulations are saved in every five minutes [Facskó *et al.*, 2016]. However, the time difference between points could be more than five minutes at the boundary of the subintervals, because the length of simulation intervals is determined in minutes. To facilitate analysis of the simulation results, all simulation data were interpolated to one minute resolution. This method

242 does not provide extra information to the cross correlation calculation. The data gaps  
 243 are eliminated using interpolation in the data and extrapolation when the gap is at the  
 244 start or the end of the selected interval. The spin resolution (4 s) of Cluster SC3 mag-  
 245 netic field measurements is averaged over one minute around ( $\pm 30\text{ s}$ ) the time stamps  
 246 of the saved data.

247 For the correlation calculation intervals are selected carefully in the solar wind, the  
 248 magnetosheath, the dayside and the night side magnetosphere. In these intervals the pa-  
 249 rameters do not varied a lot and neither the Cluster nor the virtual probe crossed any  
 250 boundary layer. To compare the shape of the  $B_z$  magnetic field,  $V_x$  solar wind speed and  
 251 the  $n_{CIS}$  and the  $n_{EFW}$  curves we calculate cross correlation on selected intervals. Some-  
 252 times we get very bad results. Then we examined carefully the case and removed the short  
 253 intervals (shorter than four hours) from the correlation calculation and large data gaps  
 254 from the correlation calculation. (The data gaps are interpolated however they cause loss  
 255 of information.) Those intervals are also neglected where the plasma instrument has cal-  
 256 ibration error or changed its mode from magnetosphere to solar wind (for example). The  
 257 electron density is also calculated using the empirical density formula (see Equation 1)  
 258 and make the correlation calculation. We want to avoid calibration errors and sudden  
 259 non-physical jumps mentioned previously. The results do not differ significantly however  
 260 the  $n_{EFW}$  has not mode change and it is applicable in the magnetosphere too (against  
 261 the CIS HIA instrument).

### 262 3.1 Solar wind

263 We use OMNI IMF and solar wind velocity, density and temperature data as in-  
 264 put of the simulation. However, it is not useless to compare the solar wind region in the  
 265 simulation and the measurements. The IMF X component cannot be given to the GUMICS-4  
 266 as input [Janhunen *et al.*, 2012; Facskó *et al.*, 2016]. However the magnetic field of the  
 267 solar wind has X component in the simulations. Additionally the solar wind structure  
 268 might change from the simulation domain boundary at  $+32 R_E$  to the sub-solar point  
 269 of the terrestrial bow shock where all OMNI data is shifted. Almost the same solar wind  
 270 intervals are used as in the see Table 1 of Facskó *et al.* [2016]. The number of these in-  
 271 tervals is small because the Cluster fleet instruments were calibrated in 2002, just after  
 272 launching (Table 1). Hence we do not have so good ion plasma data coverage for this  
 273 year. Additionally, to improve the accuracy of the correlation calculation (see below) we

274 delete those intervals which were too short (shorter than five hours) or the CIS HIA  
 275 instrument changed its mode. The Cluster fleet is located in the solar wind only from De-  
 276 cember to May and only for a couple of hours during each orbit near to the apogee. We  
 277 double check whether the Cluster SC3 stays in the solar wind in both the simulation and  
 278 the reality. We also check the omnidirectional CIS HIA ion spectra on the Cluster Sci-  
 279 ence Archive (CSA; <https://www.cosmos.esa.int/web/csa/csds-quicklook-plots>). Hence  
 280 17 intervals are remained in the solar wind to study (Figure 1).

281 The selected intervals have quiet solar wind conditions (Figure 2). The GUMICS-4  
 282 simulation results have five minutes resolution and the Cluster SC3 measurements have  
 283 one minutes resolution (Figure 3). The measurements vary significantly. Inspect of the  
 284 quiet conditions the solar wind density often changes and deviates from the simulation.  
 285 On the Figure 4c both densities deviate significantly. The CIS HIA density deviation is  
 286 larger as it is expected because of the complexity and the large number of working modes  
 287 of the CIS instrument. The magnetic field and the solar wind velocity fit better. On Fig-  
 288 ure 5a the correlation of the magnetic field is very good; furthermore on Figure 5c, 5e, 5f  
 289 the correlation of the solar wind velocity and density is excellent (Table 1). The time  
 290 shift on Figure 5bFigure 5d, Figure 5f is about five minutes for the magnetic field and  
 291 the CIS data. On Figure 5h for the EFW data the time shift is worse. It is not deter-  
 292 mined as well as the other parameters.

### 293 3.2 Magnetosheath

294 The Cluster SC3 spent only a few time in the solar wind from December, 2002 to  
 295 May, 2003. However, the orbit of the spacecraft always crosses the magnetosheath (Fig-  
 296 ure 6). We selected intervals when the value of the magnetic field is around 25 nT. The  
 297 field should be fluctuating because of the turbulent and deviated flow of the solar wind  
 298 after passing the bow shock. In the same time the solar wind temperature increases. The  
 299 solar wind speed drops it value is only 100-300 km/s. The density of the plasma flow in-  
 300 creased and reached the  $10\text{-}20 \text{ cm}^{-3}$ . The narrow band on the omnidirectional CIS HIA  
 301 ion spectra from the CSA (<https://www.cosmos.esa.int/web/csa/csds-quicklook-plots>)  
 302 is widened after passing the bow shock. After 15-30 min this passage we considered the  
 303 Cluster SC3 to be entered to the magnetosheath. At the inner boundary the flow speed  
 304 drops and the density as well. The magnetic field starts growing and it is less turbulent  
 305 than in the magnetosheath. The wide band on the the omnidirectional CIS HIA ion spec-

tra disappears. 15-30 minutes before the appearance of these indicators of the magnetopause crossing our intervals end. All intervals contain large data gap, non-physical jump of instrument mode changing or shorter than four hour are removed. Hence 74 intervals considered in our final selection (Table 2).

All intervals have quiet upstream (or input) solar wind conditions (Figure 7). Inspect of our selection the magnetic field and the plasma parameters and the calculated empirical density vary significantly stronger than in the solar wind intervals (Figure 8). The deviation of the simulated and the observed data is larger in this region as well. The scattered plots of the magnetic field, plasma flow speed and the densities agree well however these plot relatively less accurate than the scattered plots of the solar wind (Figure 9a, 9b, 9c). The correlation of the simulated and the observed data is good for the magnetic field (Figure 10a), very good for the ion plasma moments and the calculated density (Figure 10c, 10e, 10g). The timeshift of the magnetic field is within five minutes mostly (Figure 10b) however the timeshift of the ion plasma moments is scattered (Figure 10d, 10f). The timeshift of the calculated EFW density seems to be more accurate (Figure 10h). Generally, the GUMICS–4 is less accurate in the magnetosheath. The magnetic field is quite good however the plasma parameters are not so good. The calculated empirical EFW density ( $n_{EFW}$ ) fits better than the CIS HIA density ( $n_{CIS}$ ).

### 3.3 Magnetosphere

To select intervals in the magnetosphere we looked for the CIS HIA OMNI directional ionflux. When the band of the hot magnetosheath ion population (dis)appeared, the magnetosphere started/finished. The solar wind density becomes slowly zero, a magnetic field and the solar wind density drop and reach the zero value. We left 15-30 min after/before the magnetopause transition to appoint the interval in the magnetosphere. In this way we found 132 intervals in the magnetosphere (Table 3) using Cluster SC3 measurements. The Cluster SC3 spends considerable time in the magnetosphere (Figure 11).

Here we show neither any correlation calculation nor comparison plot. In the magnetosphere the GUMICS–4 does not work well. Neither the magnetic field nor the plasma moments nor the  $N_{EFW}$  fit well. The solar wind velocity does not reach zero in the simulation. Instead the solar wind enters to the night side magnetosphere. The solar wind CIS HIA ion plasma density and the calculated density from spacecraft potential increase

337 closer to the Earth (plasmasphere). The GUMICS–4 density is low there. We calculated  
 338 the dipole field in GSE using Tsyganenko geotool box [Tsyganenko, 1995] and substracted  
 339 from both the observed and the simulated magnetic field  $B_z$  data. The correlation of these  
 340 corrected magnetic field measurements and simulations is very low too.

341 **3.4 Bow shock, magnetopause, neutral sheet**

342 78 intervals are selected when the Cluster SC3 crossed the terrestrial bow shock  
 343 once or multiple times. When the spacecraft crosses the bow shock inward direction the  
 344 magnitude of the magnetic field and the solar wind density increases 4–5 times (from 5 nT  
 345 or  $5 \text{ cm}^{-3}$ , respectively), the solar wind speed drops from 400–600 km/s to 100–300 km/s;  
 346 furthermore the narrow band on the omnidirectional Cluster CIS HIA ion spectra is widened.  
 347 The Cluster measurements are 1-min averaged and the GUMICS–4 simulations has 5–  
 348 min resolution hence all bow shock transitions of the virtual spacecraft are slower and  
 349 smoother. Additionally, the multiple bow shock transitions are not visible in the GUMICS  
 350 simulations. The code reacts slowly for such sudden changes. The magnetic signatures  
 351 fit better than the calculated plasma moments. The jump of the ion plasma parameters  
 352 and the derived Cluster EFW density of the simulations are shifted to the measurements.  
 353 Generally, the density and the velocity of the simulations seem to be less accurate than  
 354 the magnetic field of the simulations.

355 56 intervals are selected around magnetopause crossings (Anekallu, private com-  
 356 munication). When the spacecraft crosses the magnetopause inward direction the mag-  
 357 nitude of the magnetic field increases, the solar wind speed drops from 100–300 km/s to  
 358 zero, the plasma density becomes zero; furthermore the wide band on the omnidirectional  
 359 Cluster CIS HIA ion spectra disappears. These changes are not so fast. The location of  
 360 the magnetopause is well determined by the Cluster SC3 measurements. However, it is  
 361 very difficult to identify the magnetopause crossings in the simulation data. The 5-min  
 362 resolution of the simulations provides smooth and averaged curves without sharp changes.  
 363 Furthermore, the magnetopause crossings very often cannot be seen in the simulations.  
 364 Or when the magnetopause crossings are clearly identified in both simulations and space-  
 365 craft measurements the events are shifted. The accuracy of the model is lower for the  
 366 dayside magnetopause locations.

367 Nine intervals are chosen around Cluster SC3 neutral sheet crossings (Figure 12;  
 368 Table 6; Tanskanen, private communication). The neutral sheets location is determined  
 369 using the results of the Boundary Layet Identification Code (BLIC) Project [Facsikó *et al.*,  
 370 in preparation]. The BLIC code determines the neutral sheet crossing Cluster FGM mag-  
 371 netic field measurements using Wang and Xu [1994]’s method. When the solar wind speed  
 372 is almost zero; furthermore the CIS HIA density and the EFW calculated density are  
 373 almost zero too; finally the GSE Z component of the magnetic field changes its sign the  
 374 code indicated neutral sheet crossing (Figure 20; red and blue curves). Surprisingly the  
 375 neutral sheet crossings are visible very well in the GUMICS simulations (Figure 20; black  
 376 curves). For five events (from nine Cluster SC3 crossings) the GUMICS–4 also provides  
 377 similar smoothed parameters and change of sign of the  $B_z$  component. This is a very good  
 378 result because the tail in the GUMICS–4 simulations is significantly smaller than the  
 379 observed [Gordeev *et al.*, 2013; Facsikó *et al.*, 2016]; furthermore the solar wind enters  
 380 in the tail in MHD simulations generally [Kallio and Facsikó, 2015].

## 381 4 Discussion

382 The agreement of the solar wind  $B_z$ ,  $V_x$  and  $n_{EFW}$  with the similar GUMICS sim-  
 383 ulation parameters is very good (Figure 4a, 4b, 4c, blue). The agreement of the  $n_{CIS}$   
 384 is worse (Figure 4c, red). It was expected because the  $n_{EFW}$  depends only the space-  
 385 craft potential provided by the EFW instrument. However, the CIS instrument has many  
 386 mode for measure the plasma parameters and it needs periodical calibration too. The  
 387 correlation of the solar wind  $V_x$ ,  $n_{CIS}$  and  $n_{EFW}$  with the similar GUMICS simulation  
 388 parameters is greater then 0.9 (Figure 5c, 5e, 5g). The correlation of the  $B_z$  is also greater  
 389 than 0.8 (Figure 5a). Both numbers prove very high correlation. The inbound wall of  
 390 the GUMICS–4 code is at  $32 R_E$  [Janhunen *et al.*, 2012], the nose of the terrestrial bow  
 391 shock is at about  $20 R_E$ . If the solar wind speed is 400 km/s, then this spatial distance  
 392 means less than 5 minutes delay, so it should not be visible. 80% of the intervals sup-  
 393 port this theory but 20 % not. In these cases the one-minute resolution  $B_z$ ,  $n_{CIS}$  or the  
 394  $n_{EFW}$  parameters have a sudden jump or variation that the simulation cannot follow,  
 395 or the resolution of the simulation data (5 minutes) is too small to see these variations.  
 396 Therefore, the correlation calculation is not accurate in these cases. Previously the OMNI  
 397 data was compared to the Cluster data and the Cluster measurements were compared  
 398 to the GUMICS–4 [Facsikó *et al.*, 2016]. The comparison suggests that the GUMICS–4

399 results should be similar with the OMNI data. Furthermore, we calculate correlation func-  
 400 tions in the solar wind, where there is no significant perturbation of the input param-  
 401 eters in the simulation box. Therefore, we get an expected result after comparing the  
 402 two different correlation calculations.

403 In the magnetosheath we get worse agreement with the GUMICS simulation data  
 404 (Figure 9a, 9b, 9c). However, it means only the larger uncertainty of the scattered plot.  
 405 The general reason of this larger uncertainty seems to the larger number of point. The  
 406 slowed down solar wind shows strong turbulence. This phenomena explains the higher  
 407 variations of the  $B_z$  magnetic field on Figure 9a. The solar wind  $V_x$ ,  $n_{CIS}$  and  $n_{EFW}$   
 408 agree better than the magnetic field component (Figure 9b, 9c). Here there is no devi-  
 409 ation between the densities derived in different ways ( $n_{CIS}$  and  $n_{EFW}$ ) on Figure 9c.  
 410 The Figure 10 seems to be contradict these statements above. The larger uncertainty  
 411 of the  $B_z$  is visible on Figure 10a. However, that correlation is still good on Figure 10b.  
 412 The other parameters have larger ( $> 0.9$ ) correlation on Figure 10c, 10e, 10g. However,  
 413 the time shifts on Figure 10d, 10f, 10h seem to be worse. Actually here the time shift  
 414 are worse because the shape of the time series in the magnetosheath looks very similar.  
 415 Hence, the correlation calculation provides larger time shifts for the ion plasma param-  
 416 eters and the  $n_{EFW}$ .

417 In the magnetosphere the GUMICS–4 does not work well. The GUMICS–4 uses  
 418 a tilted dipole to describe the terrestrial magnetic field [Janhunen *et al.*, 2012]. After re-  
 419 moving the magnetic dipole from the magnetic field measurements of the Cluster SC3  
 420 and the simulation we get very low correlations and unacceptable time shifts (not shown).  
 421 In the inner magnetosphere the tilted dipole is an insufficient description. However, the  
 422 plasma momentums and the  $N_{EFW}$  fit neither. The MHD approach lost its validity in  
 423 the inner magnetosphere domain therefore the  $V_x$  and the  $n$  of the simulations do not  
 424 agree to the  $V_x$ , the  $n_{CIS}$  and the  $n_{EFW}$  measured by the Cluster SC3. Within the  $3.7 R_E$   
 425 domain another model is necessary that contains more physics as you can see another  
 426 global MHD code [Lyon *et al.*, 2004; Raeder *et al.*, 2008; Powell *et al.*, 1999; Tóth *et al.*,  
 427 2012]. This result explains the limited accuracy of the cross polar cap potential (CPCP)  
 428 and geomagnetic indices of the GUMICS simulations [Juusola *et al.*, 2014]. The CPCP  
 429 had good agreement of GUMICS simulations and spacecraft measurements therefore this  
 430 quantity could be used for capable and relevant simulation studies [Lakka *et al.*, 2018a].  
 431 Haiducek *et al.* [2017] also made a comparison study of the geomagnetic indices and the

432 CPCP. The Space Weather Modelling Framework (SWMF) was tested. When the in-  
 433 inner magnetosphere model was switched off in the simulation the only the comparison of  
 434 the simulated and observed CPCP was good. Therefore, the reason of the discrepancy  
 435 of the geomagnetic indices in the GUMICS simulations must be the missing inner mag-  
 436 netosphere model.

437 The reason of the disagree of the simulation results and the measurements could  
 438 be the code or the bad input parameters. During the 1-year run the distributions of the  
 439 OMNI solar wind magnetic field  $B_x$ ,  $B_y$ ,  $B_z$  components (Figure 13a, 13b, 13c); solar  
 440 wind velocity  $V_x$ ,  $V_y$ ,  $V_z$  components (Figure 13d, 13e, 13f) and the solar wind  $P$  dynamic  
 441 pressure are calculated (Figure 13g) from January 29, 2002 to February 2, 2003 in GSE  
 442 reference frame. The intervals when the GUMICS–4 simulations and the Cluster SC3  
 443 measurements disagreed are collected for intervals in the solar wind (Table 4) and the  
 444 magnetosheath (Table 5). The averaged shifted OMNI parameters of the badly agree in-  
 445 tervals from the Tables 4 and 5 are saved. The distributions of the OMNI parameters  
 446 belong to the bad simulation results are calculated for the solar wind region (Figure 14, 15 and 16)  
 447 and in the magnetosheath (Figure 17, 18 and 19).

448 The badness of the GUMICS-4 simulations does not depend on the OMNI param-  
 449 eters in the solar wind and magnetosheath regions. For the magnetosphere the same study  
 450 does not need to be done because the deviance of the measurements and the simulations  
 451 is so large that it cannot be caused by the wrong OMNI solar wind parameters.

452 The bow shock locations agree in the GUMICS simulations and the Cluster SC3  
 453 measurements. However, the magnetopause locations do not fit as good as the bow shock  
 454 in simulations and observations. In simulations the location of the magnetopause is de-  
 455 termined by currents densities or particle density gradients [García and Hughes, 2007;  
 456 Gordeev *et al.*, 2013, see references therein]. In this paper the previously saved simula-  
 457 tion parameters along the virtual Cluster SC3 orbit are analysed. Therefore, the above  
 458 mentioned methods cannot be applied. The reason of the inaccuracy of the magnetopause  
 459 positions in the simulations must be the missing inner magnetosphere and ring current  
 460 module. This discrepancy of the magnetopause location agrees with the results of Gordeev  
 461 *et al.* [2013] and Fácskó *et al.* [2016]. Gordeev *et al.* [2013] compared synthetic GUMICS  
 462 runs with empirical formula of the magnetopause locations. Fácskó *et al.* [2016] used OMNI

463 solar wind data as input and got the same result as *Gordeev et al.* [2013] and this pa-  
 464 per.

465 Surprisingly the neutral sheets are visible in both simulations and observations (Fig-  
 466 ure 20, Table 6). This experience is exceptional because the night side magnetosphere  
 467 of the GUMICS–4 simulations is small and twisted [*Gordeev et al.*, 2013; *Facskó et al.*,  
 468 2016]. However, in this cases the IMF has no large  $B_y$  component. From *Facskó et al.*  
 469 [2016] we know that the GUMICS has normal long tail (or night side magnetosphere)  
 470 if the  $B_y$  is small.

## 471 5 Summary and conclusions

472 Bla-bla-bla

### 473 Acknowledgments

474 The OMNI data were obtained from the GSFC/SPDF OMNIWeb interface at <http://omniweb.gsfc.nasa.gov>.  
 475 The authors thank the FGM Team (PI: Chris Carr), the CIS Team (PI: Iannis Dandouras),  
 476 the WHISPER Team (PI: Jean-Louis Rauch), the EFW Team (PI: Mats Andre) and the  
 477 Cluster Science Archive for providing FGM magnetic field, CIS HIA ion plasma and WHIS-  
 478 PER electron density measurements. Data analysis was partly done with the QSAS sci-  
 479 ence analysis system provided by the United Kingdom Cluster Science Centre (Impe-  
 480 rial College London and Queen Mary, University of London) supported by the Science  
 481 and Technology Facilities Council (STFC). Eija Tanskanen acknowledges financial sup-  
 482 port from the Academy of Finland for the ReSoLVE Centre of Excellence (project No. 272157).  
 483 Gábor Facskó thanks Anna-Mária Vígh for improving the English of the paper. The au-  
 484 thors thank Pekka Janhunen for developing the GUMICS–4 code; furthermore Minna  
 485 Palmroth and Zoltán Vörös for the useful discussions. The work of Gábor Facskó was  
 486 supported by mission science funding for the Van Allen Probes mission, the American  
 487 Geophysical Union and the HAS Research Centre for Astronomy and Earth Sciences,  
 488 Sopron, Hungary. For further use of the year run data, please contact Minna Palmroth  
 489 ([minna.palmroth@helsinki.fi](mailto:minna.palmroth@helsinki.fi)) or use the archive of the Community Coordinated Mod-  
 490 elling Center ([https://ccmc.gsfc.nasa.gov/publications/posted\\_runs/FacskoEA2016.php](https://ccmc.gsfc.nasa.gov/publications/posted_runs/FacskoEA2016.php)).

491

492      **References**

- 493      Balogh, A., M. W. Dunlop, S. W. H. Cowley, D. J. Southwood, J. G. Thomlinson,  
 494      K. H. Glassmeier, G. Musmann, H. Luhr, S. Buchert, M. H. Acuna, D. H. Fair-  
 495      field, J. A. Slavin, W. Riedler, K. Schwingenschuh, and M. G. Kivelson (1997),  
 496      The Cluster Magnetic Field Investigation, *Space Science Reviews*, 79, 65–91, doi:  
 497      10.1023/A:1004970907748.
- 498      Balogh, A., C. M. Carr, M. H. Acuña, M. W. Dunlop, T. J. Beek, P. Brown,  
 499      K. Fornaçon, E. Georgescu, K. Glassmeier, J. Harris, G. Musmann, T. Oddy, and  
 500      K. Schwingenschuh (2001), The Cluster Magnetic Field Investigation: overview of  
 501      in-flight performance and initial results, *Annales Geophysicae*, 19, 1207–1217.
- 502      Bartels, J., N. H. Heck, and H. F. Johnston (1939), The three-hour-range index mea-  
 503      suring geomagnetic activity, *Terrestrial Magnetism and Atmospheric Electricity*  
 504      (*Journal of Geophysical Research*), 44, 411, doi:10.1029/TE044i004p00411.
- 505      Blagau, A., I. Dandouras, A. Barthe, S. Brunato, G. Facskó, and V. Constanti-  
 506      nescu (2013), In-flight calibration of Hot Ion Analyser onboard Cluster, *Geo-  
 507      scientific Instrumentation, Methods and Data Systems Discussions*, 3, 407–435,  
 508      doi:10.5194/gid-3-407-2013.
- 509      Blagau, A., I. Dandouras, A. Barthe, S. Brunato, G. Facskó, and V. Constantinescu  
 510      (2014), In-flight calibration of the Hot Ion Analyser on board Cluster, *Geoscientific  
 511      Instrumentation, Methods and Data Systems*, 3, 49–58, doi:10.5194/gi-3-49-  
 512      2014.
- 513      Credland, J., G. Mecke, and J. Ellwood (1997), The Cluster Mission: ESA'S  
 514      Spacefleet to the Magnetosphere, *Space Science Reviews*, 79, 33–64, doi:  
 515      10.1023/A:1004914822769.
- 516      Davis, T. N., and M. Sugiura (1966), Auroral electrojet activity index AE and its  
 517      universal time variations, *Journal of Geophysical Research*, 71, 785–801, doi:  
 518      10.1029/JZ071i003p00785.
- 519      Décréau, P. M. E., P. Fergeau, V. Krasnoselskikh, E. Le Guirriec, M. Lévéque,  
 520      P. Martin, O. Randriamboarison, J. L. Rauch, F. X. Sené, H. C. Séran, J. G.  
 521      Trotignon, P. Canu, N. Cornilleau, H. de Féraudy, H. Alleyne, K. Yearby, P. B.  
 522      Mögensen, G. Gustafsson, M. André, D. C. Gurnett, F. Darrouzet, J. Lemaire,  
 523      C. C. Harvey, P. Travnicek, and Whisper Experimenters Group (2001), Early re-  
 524      sults from the Whisper instrument on Cluster: an overview, *Annales Geophysicae*,

- 525                   19, 1241–1258, doi:10.5194/angeo-19-1241-2001.
- 526                   Escoubet, C. P., M. Fehringer, and M. Goldstein (2001), Introduction The Cluster  
527                   mission, *Annales Geophysicae*, 19, 1197–1200, doi:10.5194/angeo-19-1197-2001.
- 528                   Facskó, G., I. Honkonen, T. Živković, L. Palin, E. Kallio, K. Ågren, H. Opgenoorth,  
529                   E. I. Tanskanen, and S. Milan (2016), One year in the Earth’s magnetosphere: A  
530                   global MHD simulation and spacecraft measurements, *Space Weather*, 14, 351–  
531                   367, doi:10.1002/2015SW001355.
- 532                   Facskó, G., T. B. Balogh, E. I. Anekallu, C. R. and Tanskanen, P. Peitso, L. Degener,  
533                   M. Kangwa, T. Laitinen, and S. Laakso, H. Burley (in preparation), Bow shock  
534                   identification in cluster measurements, *Space Weather*.
- 535                   Fazakerley, A. N., A. D. Lahiff, R. J. Wilson, I. Rozum, C. Anekallu, M. West, and  
536                   H. Bacai (2010a), PEACE Data in the Cluster Active Archive, *Astrophysics and  
537                   Space Science Proceedings*, 11, 129–144, doi:10.1007/978-90-481-3499-1\_8.
- 538                   Fazakerley, A. N., A. D. Lahiff, I. Rozum, D. Kataria, H. Bacai, C. Anekallu,  
539                   M. West, and A. Åsnes (2010b), Cluster-PEACE In-flight Calibration Status,  
540                   *Astrophysics and Space Science Proceedings*, 11, 281–299, doi:10.1007/978-90-481-  
541                   3499-1\_19.
- 542                   García, K. S., and W. J. Hughes (2007), Finding the Lyon-Fedder-Mobarry mag-  
543                   netopause: A statistical perspective, *Journal of Geophysical Research (Space  
544                   Physics)*, 112(A6), A06229, doi:10.1029/2006JA012039.
- 545                   Gordeev, E., G. Facskó, V. Sergeev, I. Honkonen, M. Palmroth, P. Janhunen, and  
546                   S. Milan (2013), Verification of the GUMICS-4 global MHD code using empirical  
547                   relationships, *Journal of Geophysical Research (Space Physics)*, 118, 3138–3146,  
548                   doi:10.1002/jgra.50359.
- 549                   Greenwald, R. A., K. B. Baker, J. R. Dudeney, M. Pinnock, T. B. Jones, E. C.  
550                   Thomas, J.-P. Villain, J.-C. Cerisier, C. Senior, C. Hanuise, R. D. Hunsucker,  
551                   G. Sofko, J. Koehler, E. Nielsen, R. Pellinen, A. D. M. Walker, N. Sato,  
552                   and H. Yamagishi (1995), Darn/Superdarn: A Global View of the Dynam-  
553                   ics of High-Latitude Convection, *Space Science Reviews*, 71, 761–796, doi:  
554                   10.1007/BF00751350.
- 555                   Guild, T. B., H. E. Spence, E. L. Kepko, V. Merkin, J. G. Lyon, M. Wilberger, and  
556                   C. C. Goodrich (2008a), Geotail and LFM comparisons of plasma sheet clima-  
557                   tology: 1. Average values, *Journal of Geophysical Research (Space Physics)*, 113,

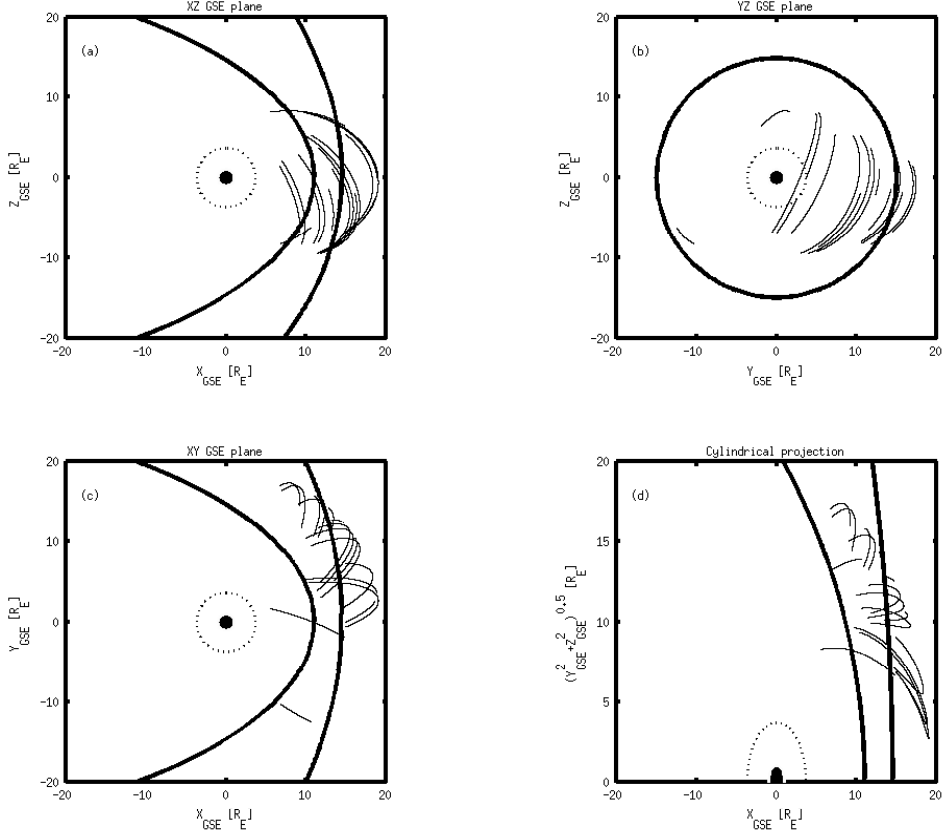
- 558 A04216, doi:10.1029/2007JA012611.
- 559 Guild, T. B., H. E. Spence, E. L. Kepko, V. Merkin, J. G. Lyon, M. Wiltberger, and  
560 C. C. Goodrich (2008b), Geotail and LFM comparisons of plasma sheet climatol-  
561 ogy: 2. Flow variability, *Journal of Geophysical Research (Space Physics)*, 113,  
562 A04217, doi:10.1029/2007JA012613.
- 563 Gustafsson, G., R. Bostrom, B. Holback, G. Holmgren, A. Lundgren, K. Stasiewicz,  
564 L. Ahlen, F. S. Mozer, D. Pankow, P. Harvey, P. Berg, R. Ulrich, A. Pedersen,  
565 R. Schmidt, A. Butler, A. W. C. Fransen, D. Klinge, M. Thomsen, C.-G. Faltham-  
566 mar, P.-A. Lindqvist, S. Christenson, J. Holtet, B. Lybekk, T. A. Sten, P. Tan-  
567 skanen, K. Lappalainen, and J. Wygant (1997), The Electric Field and Wave  
568 Experiment for the Cluster Mission, *Space Science Reviews*, 79, 137–156, doi:  
569 10.1023/A:1004975108657.
- 570 Gustafsson, G., M. André, T. Carozzi, A. I. Eriksson, C.-G. Fälthammar, R. Grard,  
571 G. Holmgren, J. A. Holtet, N. Ivchenko, T. Karlsson, Y. Khotyaintsev, S. Klimov,  
572 H. Laakso, P.-A. Lindqvist, B. Lybekk, G. Marklund, F. Mozer, K. Mursula,  
573 A. Pedersen, B. Popielawska, S. Savin, K. Stasiewicz, P. Tanskanen, A. Vaivads,  
574 and J.-E. Wahlund (2001), First results of electric field and density observations  
575 by Cluster EFW based on initial months of operation, *Annales Geophysicae*, 19,  
576 1219–1240, doi:10.5194/angeo-19-1219-2001.
- 577 Haiducek, J. D., D. T. Welling, N. Y. Ganushkina, S. K. Morley, and D. S. Oz-  
578 turk (2017), SWMF Global Magnetosphere Simulations of January 2005: Geo-  
579 magnetic Indices and Cross-Polar Cap Potential, *Space Weather*, 15, 1567–1587,  
580 doi:10.1002/2017SW001695.
- 581 Iyemori, T. (1990), Storm-time magnetospheric currents inferred from mid-latitude  
582 geomagnetic field variations, *Journal of Geomagnetism and Geoelectricity*, 42,  
583 1249–1265, doi:10.5636/jgg.42.1249.
- 584 Janhunen, P., M. Palmroth, T. Laitinen, I. Honkonen, L. Juusola, G. Facskó, and  
585 T. I. Pulkkinen (2012), The GUMICS-4 global MHD magnetosphere-ionosphere  
586 coupling simulation, *Journal of Atmospheric and Solar-Terrestrial Physics*, 80,  
587 48–59, doi:10.1016/j.jastp.2012.03.006.
- 588 Johnstone, A. D., C. Alsop, S. Burge, P. J. Carter, A. J. Coates, A. J. Coker, A. N.  
589 Fazakerley, M. Grande, R. A. Gowen, C. Gurgiolo, B. K. Hancock, B. Narheim,  
590 A. Preece, P. H. Sheather, J. D. Winningham, and R. D. Woodliffe (1997), Peace:

- 591 a Plasma Electron and Current Experiment, *Space Science Reviews*, 79, 351–398,  
592 doi:10.1023/A:1004938001388.
- 593 Juusola, L., O. Amm, K. Kauristie, and A. Viljanen (2007), A model for estimating  
594 the relation between the Hall to Pedersen conductance ratio and ground magnetic  
595 data derived from CHAMP satellite statistics, *Annales Geophysicae*, 25, 721–736,  
596 doi:10.5194/angeo-25-721-2007.
- 597 Juusola, L., G. Facskó, I. Honkonen, P. Janhunen, H. Vanhamäki, K. Kauristie,  
598 T. V. Laitinen, S. E. Milan, M. Palmroth, E. I. Tanskanen, and A. Viljanen  
599 (2014), Statistical comparison of seasonal variations in the GUMICS-4 global  
600 MHD model ionosphere and measurements, *Space Weather*, 12, 582–600, doi:  
601 10.1002/2014SW001082.
- 602 Kallio, E., and G. Facskó (2015), Properties of plasma near the moon in the magne-  
603 totail, *Planetary and Space Science*, 115, 69–76, doi:10.1016/j.pss.2014.11.007.
- 604 Kokubun, S., T. Yamamoto, M. H. Acuña, K. Hayashi, K. Shiokawa, and H. Kawano  
605 (1994), The GEOTAIL Magnetic Field Experiment., *Journal of Geomagnetism*  
606 and *Geoelectricity*, 46, 7–21, doi:10.5636/jgg.46.7.
- 607 Lakka, A., T. I. Pulkkinen, A. P. Dimmock, M. Myllys, I. Honkonen, and M. Palm-  
608 roth (2018a), The Cross-Polar Cap Saturation in GUMICS-4 During High Solar  
609 Wind Driving, *Journal of Geophysical Research (Space Physics)*, 123, 3320–3332,  
610 doi:10.1002/2017JA025054.
- 611 Lakka, A., T. I. Pulkkinen, A. P. Dimmock, E. Kilpua, M. Ala-Lahti, I. Honko-  
612 nen, M. Palmroth, and Raukunen (2018b), Icme impact at earth with low and  
613 typical mach number plasma characteristics, *Annales Geophysicae Discussions*,  
614 <https://doi.org/10.5194/angeo-2018-81>.
- 615 Lani, A., A. Sanna, N. Villedieu, and M. Panesi (2012), COOLFluiD an Open Com-  
616 putational Platform for Aerothermodynamics and Flow-Radiation Coupling, in  
617 *ESA Special Publication, ESA Special Publication*, vol. 714, p. 45.
- 618 Lyon, J. G., J. A. Fedder, and C. M. Mobarry (2004), The Lyon-Fedder-Mobarry  
619 (LFM) global MHD magnetospheric simulation code, *Journal of Atmospheric and*  
620 *Solar-Terrestrial Physics*, 66, 1333–1350, doi:10.1016/j.jastp.2004.03.020.
- 621 Mejnertsen, L., J. P. Eastwood, J. P. Chittenden, and A. Masters (2016), Global  
622 MHD simulations of Neptune’s magnetosphere, *Journal of Geophysical Research*  
623 (*Space Physics*), 121(8), 7497–7513, doi:10.1002/2015JA022272.

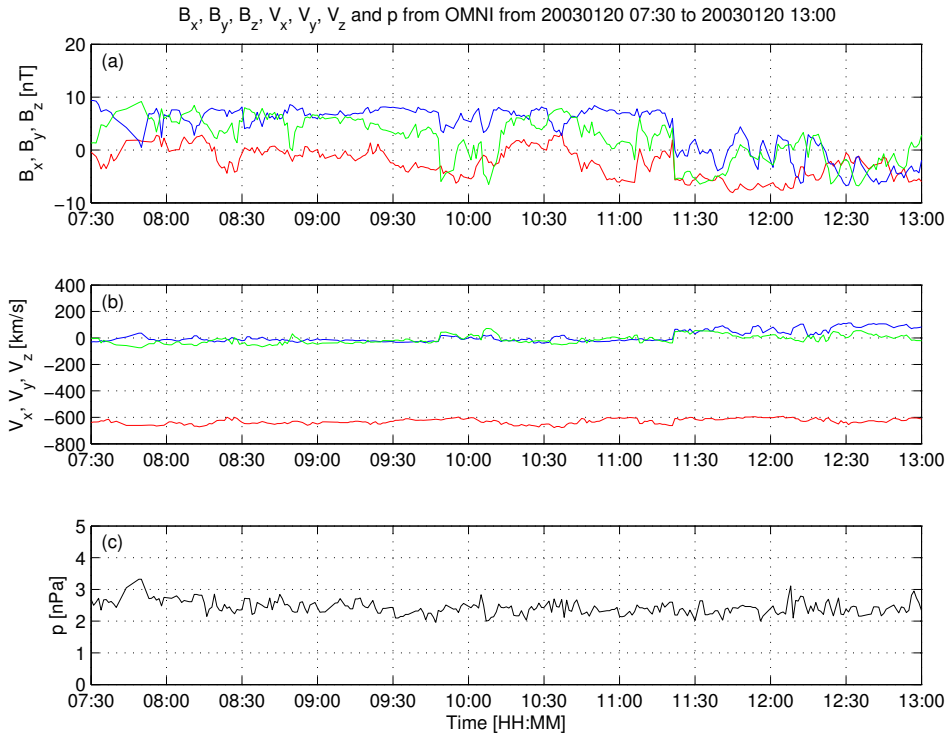
- 624 Mejnertsen, L., J. P. Eastwood, H. Hietala, S. J. Schwartz, and J. P. Chittenden  
 625 (2018), Global MHD Simulations of the Earth's Bow Shock Shape and Motion  
 626 Under Variable Solar Wind Conditions, *Journal of Geophysical Research (Space*  
 627 *Physics)*, 123(1), 259–271, doi:10.1002/2017JA024690.
- 628 Mukai, T., S. Machida, Y. Saito, M. Hirahara, T. Terasawa, N. Kaya, T. Obara,  
 629 M. Ejiri, and A. Nishida (1994), The Low Energy Particle (LEP) Experiment on-  
 630 board the GEOTAIL Satellite., *Journal of Geomagnetism and Geoelectricity*, 46,  
 631 669–692, doi:10.5636/jgg.46.669.
- 632 Peredo, M., J. A. Slavin, E. Mazur, and S. A. Curtis (1995), Three-dimensional po-  
 633 sition and shape of the bow shock and their variation with Alfvénic, sonic and  
 634 magnetosonic Mach numbers and interplanetary magnetic field orientation, *Jour-*  
 635 *nal of Geophysical Research*, 100, 7907–7916, doi:10.1029/94JA02545.
- 636 Powell, K. G., P. L. Roe, T. J. Linde, T. I. Gombosi, and D. L. De Zeeuw (1999), A  
 637 Solution-Adaptive Upwind Scheme for Ideal Magnetohydrodynamics, *Journal of*  
 638 *Computational Physics*, 154, 284–309, doi:10.1006/jcph.1999.6299.
- 639 Raeder, J., D. Larson, W. Li, E. L. Kepko, and T. Fuller-Rowell (2008), OpenG-  
 640 GCM Simulations for the THEMIS Mission, *Space Science Reviews*, 141, 535–555,  
 641 doi:10.1007/s11214-008-9421-5.
- 642 Reigber, C., H. Lühr, and P. Schwintzer (2002), CHAMP mission status, *Advances*  
 643 *in Space Research*, 30, 129–134, doi:10.1016/S0273-1177(02)00276-4.
- 644 Reme, H., J. M. Bosqued, J. A. Sauvaud, A. Cros, J. Dandouras, C. Aoustin,  
 645 J. Bouyssou, T. Camus, J. Cuvilo, C. Martz, J. L. Medale, H. Perrier, D. Rome-  
 646 fort, J. Rouzaud, C. D'Uston, E. Mobius, K. Crocker, M. Granoff, L. M. Kistler,  
 647 M. Popecki, D. Hovestadt, B. Klecker, G. Paschmann, M. Scholer, C. W. Carl-  
 648 son, D. W. Curtis, R. P. Lin, J. P. McFadden, V. Formisano, E. Amata, M. B.  
 649 Bavassano-Cattaneo, P. Baldetti, G. Belluci, R. Bruno, G. Chionchio, A. di Lel-  
 650 lis, E. G. Shelley, A. G. Ghielmetti, W. Lennartsson, A. Korth, H. Rosenbauer,  
 651 R. Lundin, S. Olsen, G. K. Parks, M. McCarthy, and H. Balsiger (1997), The  
 652 Cluster Ion Spectrometry (CIS) Experiment, *Space Science Reviews*, 79, 303–350,  
 653 doi:10.1023/A:1004929816409.
- 654 Rème, H., C. Aoustin, J. M. Bosqued, I. Dandouras, B. Lavraud, J. A. Sauvaud,  
 655 A. Barthe, J. Bouyssou, T. Camus, O. Coeur-Joly, A. Cros, J. Cuvilo, F. Ducay,  
 656 Y. Garbarowitz, J. L. Medale, E. Penou, H. Perrier, D. Romefort, J. Rouzaud,

- 657 C. Vallat, D. Alcayd, C. Jacquay, C. Mazelle, C. D'Uston, E. Mobius, L. M.  
 658 Kistler, K. Crocker, M. Granoff, C. Mouikis, M. Popecki, M. Vosbury, B. Klecker,  
 659 D. Hovestadt, H. Kucharek, E. Kuenneth, G. Paschmann, M. Scholer, N. Sckopke,  
 660 E. Seidenschwang, C. W. Carlson, D. W. Curtis, C. Ingraham, R. P. Lin, J. P.  
 661 McFadden, G. K. Parks, T. Phan, V. Formisano, E. Amata, M. B. Bavassano-  
 662 Cattaneo, P. Baldetti, R. Bruno, G. Chionchio, A. di Lellis, M. F. Marcucci,  
 663 G. Pallocchia, A. Korth, P. W. Daly, B. Graeve, H. Rosenbauer, V. Vasyliunas,  
 664 M. McCarthy, M. Wilber, L. Eliasson, R. Lundin, S. Olsen, E. G. Shelley, S. Fuseli-  
 665 ler, A. G. Ghielmetti, W. Lennartsson, C. P. Escoubet, H. Balsiger, R. Friedel, J.-  
 666 B. Cao, R. A. Kovrashkin, I. Papamastorakis, R. Pellat, J. Scudder, and B. Son-  
 667 nerup (2001), First multispacecraft ion measurements in and near the Earth's  
 668 magnetosphere with the identical Cluster ion spectrometry (CIS) experiment,  
 669 *Annales Geophysicae*, 19, 1303–1354, doi:10.5194/angeo-19-1303-2001.
- 670 Ritter, P., H. Luir, A. Viljanen, O. Amm, A. Pulkkinen, and I. Sillanpa (2004),  
 671 Ionospheric currents estimated simultaneously from CHAMP satelliteand IMAGE  
 672 ground-based magnetic field measurements: a statisticalstudy at auroral latitudes,  
 673 *Annales Geophysicae*, 22, 417–430, doi:10.5194/angeo-22-417-2004.
- 674 Rostoker, G. (1972), Geomagnetic indices., *Reviews of Geophysics and Space  
 Physics*, 10, 935–950, doi:10.1029/RG010i004p00935.
- 675 Sofko, G. J., R. Greenwald, and W. Bristow (1995), Direct determination of large-  
 676 scale magnetospheric field-aligned currents with SuperDARN, *Geophysical Re-  
 677 search Letters*, 22, 2041–2044, doi:10.1029/95GL01317.
- 678 Thomsen, M. F. (2004), Why Kp is such a good measure of magnetospheric convec-  
 679 tion, *Space Weather*, 2, S11004, doi:10.1029/2004SW000089.
- 680 Toth, G., I. V. Sokolov, T. I. Gombosi, D. R. Chesney, C. R. Clauer, D. L. de  
 681 Zeeuw, K. C. Hansen, K. J. Kane, W. B. Manchester, R. C. Oehmke, K. G. Pow-  
 682 ell, A. J. Ridley, I. I. Roussev, Q. F. Stout, O. Volberg, R. A. Wolf, S. Sazykin,  
 683 A. Chan, B. Yu, and J. Kota (2005), Space Weather Modeling Framework: A  
 684 new tool for the space science community, *Journal of Geophysical Research (Space  
 Physics)*, 110, A12226, doi:10.1029/2005JA011126.
- 685 Toth, G., B. van der Holst, I. V. Sokolov, D. L. De Zeeuw, T. I. Gombosi, F. Fang,  
 686 W. B. Manchester, X. Meng, D. Najib, K. G. Powell, Q. F. Stout, A. Glo-  
 687 cer, Y.-J. Ma, and M. Opher (2012), Adaptive numerical algorithms in space

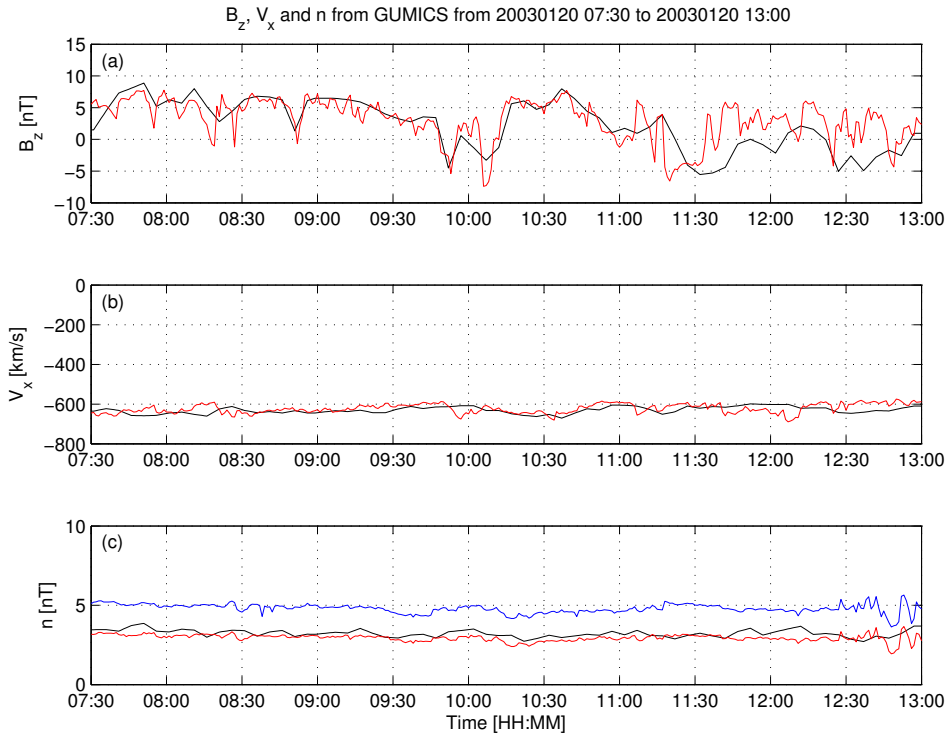
- 690 weather modeling, *Journal of Computational Physics*, 231, 870–903, doi:  
691 10.1016/j.jcp.2011.02.006.
- 692 Trotignon, J. G., P. M. E. Décréau, J. L. Rauch, X. Vallières, A. Rochel,  
693 S. Kougblénou, G. Lointier, G. Facskó, P. Canu, F. Darrouzet, and A. Masson  
694 (2010), The WHISPER Relaxation Sounder and the CLUSTER Active Archive,  
695 *Astrophysics and Space Science Proceedings*, 11, 185–208, doi:10.1007/978-90-481-  
696 3499-1\_12.
- 697 Trotignon, J.-G., Vallières, and the WHISPER team (2011), Calibration report of  
698 the whisper measurements in the cluster active archive (caa), *Tech. rep.*, LPC2E  
699 CNRS, caa-est-cr-whi.
- 700 Tsyganenko, N. A. (1995), Modeling the Earth's magnetospheric magnetic field  
701 confined within a realistic magnetopause, *Journal of Geophysical Research*, 100,  
702 5599–5612, doi:10.1029/94JA03193.
- 703 Vörös, Z., G. Facskó, M. Khodachenko, I. Honkonen, P. Janhunen, and M. Palmroth  
704 (2014), Windsock memory COnditioned RAM (CO-RAM) pressure effect: Forced  
705 reconnection in the Earth's magnetotail, *Journal of Geophysical Research (Space*  
706 *Physics)*, 119, 6273–6293, doi:10.1002/2014JA019857.
- 707 Wang, Z.-D., and R. L. Xu (1994), Signatures of the magnetotail neutral sheet,  
708 *Geophysical Research Letters*, 21(19), 2087–2090, doi:10.1029/94GL01960.
- 709 Weimer, D. R. (2005), Improved ionospheric electrodynamic models and applica-  
710 tion to calculating Joule heating rates, *Journal of Geophysical Research (Space*  
711 *Physics)*, 110, A05306, doi:10.1029/2004JA010884.
- 712 Wiltberger, M., E. J. Rigler, V. Merkin, and J. G. Lyon (2017), Structure of High  
713 Latitude Currents in Magnetosphere-Ionosphere Models, *Space Science Reviews*,  
714 206, 575–598, doi:10.1007/s11214-016-0271-2.
- 715 Zhang, B., W. Lotko, M. J. Wiltberger, O. J. Brambles, and P. A. Damiano (2011),  
716 A statistical study of magnetosphere-ionosphere coupling in the Lyon-Fedder-  
717 Mobarry global MHD model, *Journal of Atmospheric and Solar-Terrestrial*  
718 *Physics*, 73, 686–702, doi:10.1016/j.jastp.2010.09.027.



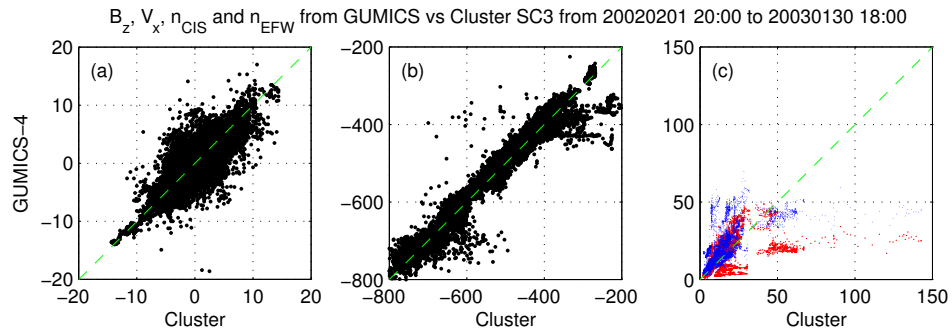
719 **Figure 1.** Cluster SC3 orbit in the solar wind in GSE system for all intervals (see Table 1).  
 720 (a) XZ (b) YZ (c) XY (d) Cylindrical projection. Average bow-shock and magnetopause posi-  
 721 tions are drawn on all plots using solid line [Perego *et al.*, 1995; Tsyganenko, 1995, respectively].  
 722 The black dots at  $3.7 R_E$  show the boundary of the GUMICS-4 inner magnetospheric domain.  
 723 The black circle in the origo of all plots shows the size of the Earth.



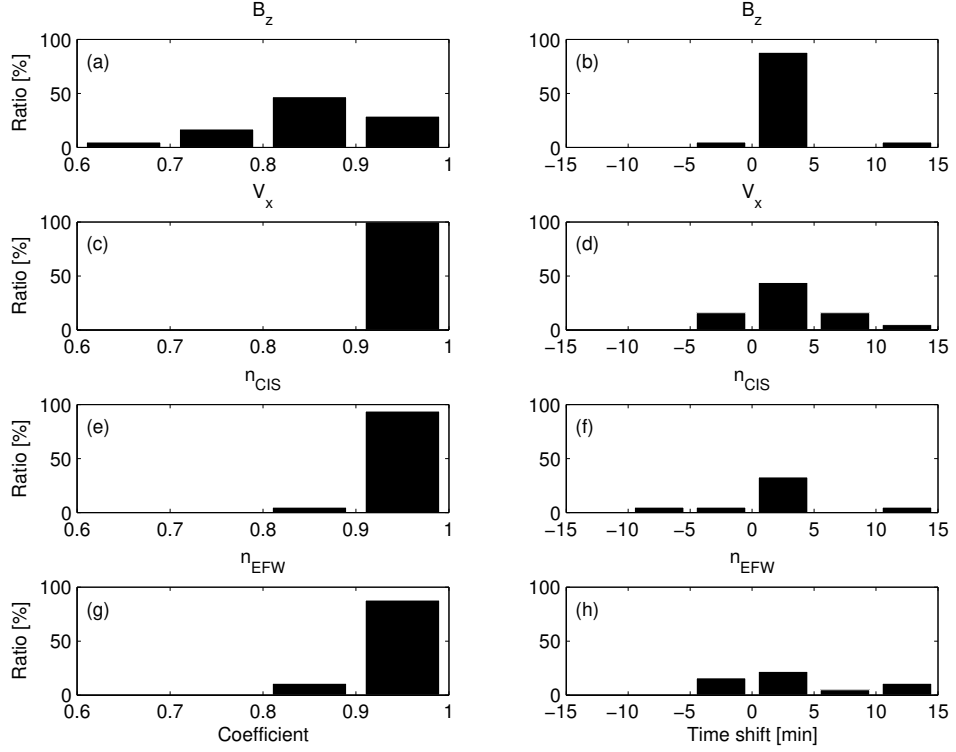
724 **Figure 2.** OMNI solar wind data in GSE system from 7:30 to 13:00 (UT) on January 20,  
 725 2003. (a) Magnetic field  $B_x$  (red),  $B_y$  (green) and  $B_z$  (blue) components. (b) Solar wind velocity  
 726  $V_x$  (red),  $V_y$  (green) and  $V_z$  (blue) components. (c) The  $P$  pressure of the solar wind (black).



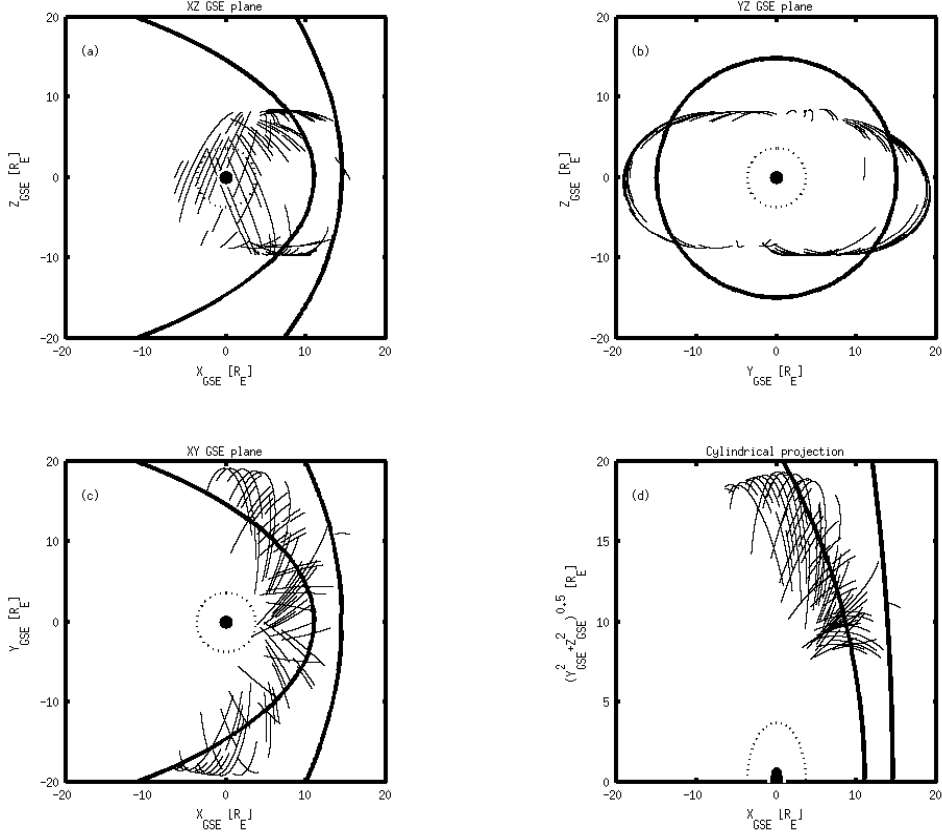
727      **Figure 3.** GUMICS-4 simulation results (black) and Cluster SC3 magnetic field, ion plasma  
 728      moments (red) and electron density calculated from spacecraft potential (blue) from January 20,  
 729      2003 from 7:30 to 13:00 (UT) in the solar wind in GSE system. (a) Magnetic field Z component.  
 730      (b) Solar wind velocity X component (c) Solar wind density.



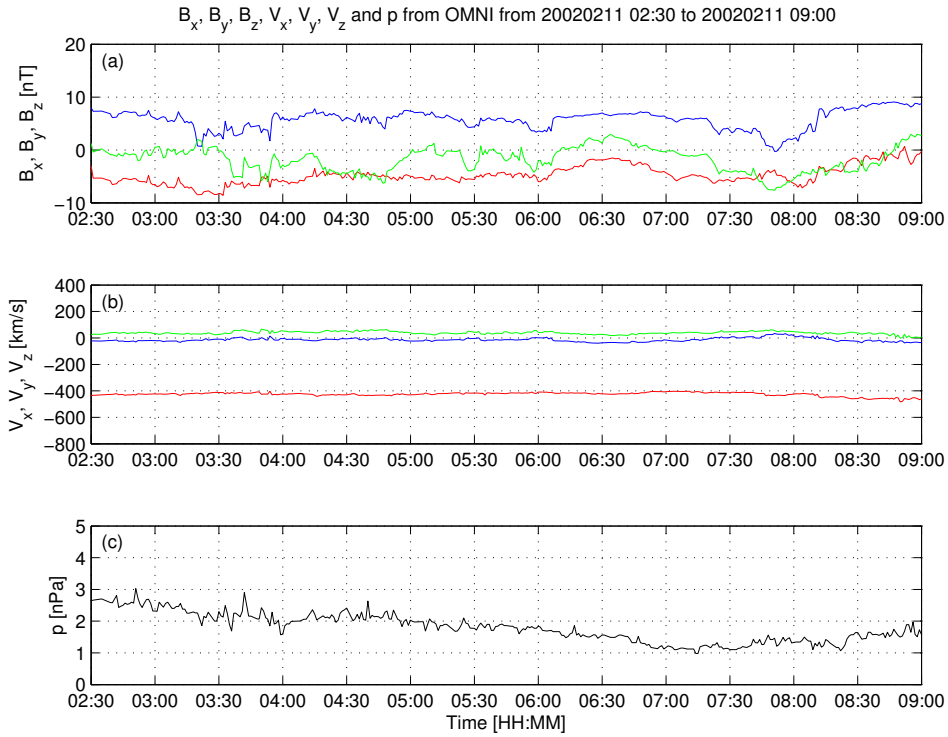
731 **Figure 4.** Scattered plots of the Cluster SC3 and GUMICS-4 simulations for all intervals in  
 732 the solar wind. The dashed line is the  $y=x$  line. (a) Magnetic field Z component in GSE system.  
 733 (b) Solar wind velocity X component in GSE system. (c) Solar wind density measured by the  
 734 CIS HIA instrument (red) and calculated from the spacecraft potential (blue).



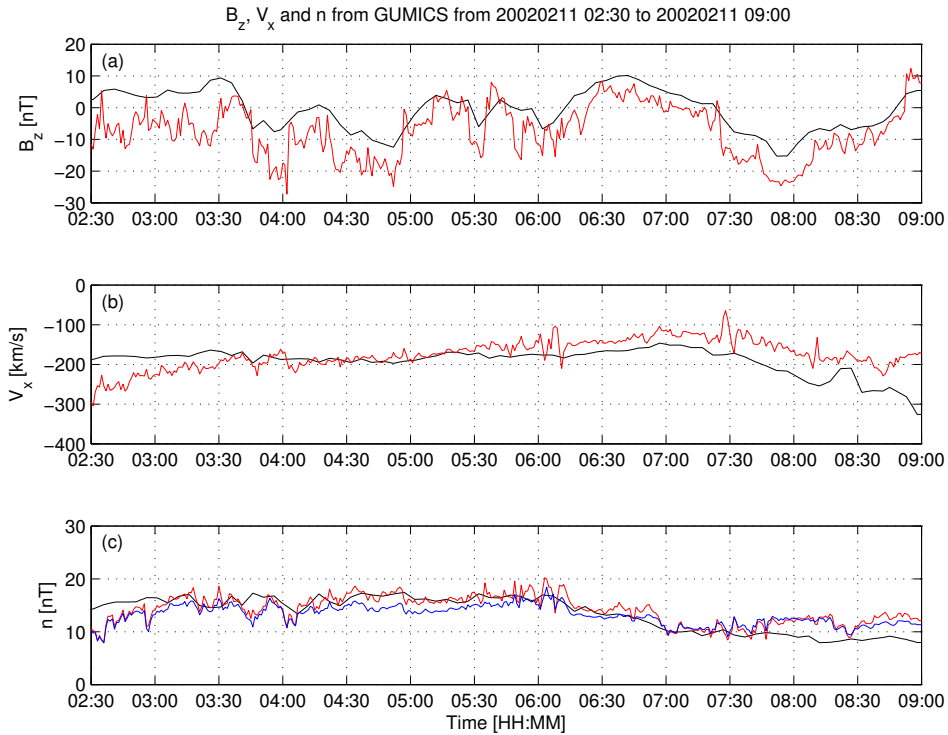
735      **Figure 5.** The distributions of the correlation coefficients (a, c, e, g) of the magnetic field Z  
 736      component ( $B_z$ ) in GSE system, solar wind velocity X component ( $V_x$ ) in GSE system, the solar  
 737      wind density measured by the CIS HIA ( $n_{CIS}$ ) instrument and calculated from the spacecraft  
 738      potential ( $n_{EFW}$ ), respectively, for all intervals in the solar wind. The distributions of the time  
 739      shifts (b, d, f, h) of the  $B_z$ , the  $V_x$ , the  $n_{CIS}$  and the  $n_{EFW}$ , respectively, for all intervals in the  
 740      solar wind.



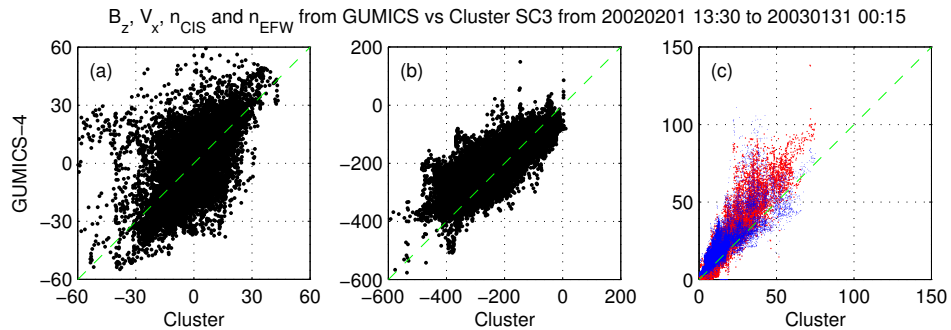
741      **Figure 6.** Cluster SC3 orbit in the magnetosheath in GSE system for all intervals (see Ta-  
 742      ble 2). (a) XZ (b) YZ (c) XY (d) Cylindrical projection. Average bow-shock and magnetopause  
 743      positions are drawn on all plots using solid line [Peredo *et al.*, 1995; Tsyganenko, 1995, respec-  
 744      tively]. The black dots at  $3.7 R_E$  show the boundary of the GUMICS-4 inner magnetospheric  
 745      domain. The black circle in the origo of all plots shows the size of the Earth.



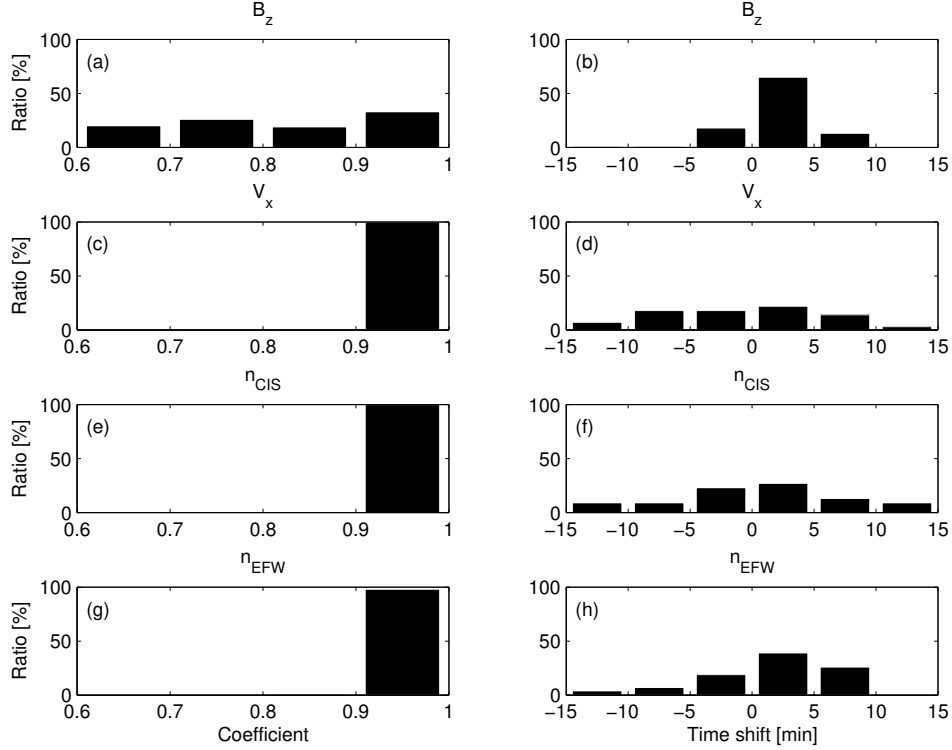
746 **Figure 7.** OMNI solar wind data in GSE system from 2:30 to 09:00 (UT) on February 11,  
 747 2002. (a) Magnetic field  $B_x$  (red),  $B_y$  (green) and  $B_z$  (blue) components. (b) Solar wind velocity  
 748  $V_x$  (red),  $V_y$  (green) and  $V_z$  (blue) components. (c) The  $P$  pressure of the solar wind (black).



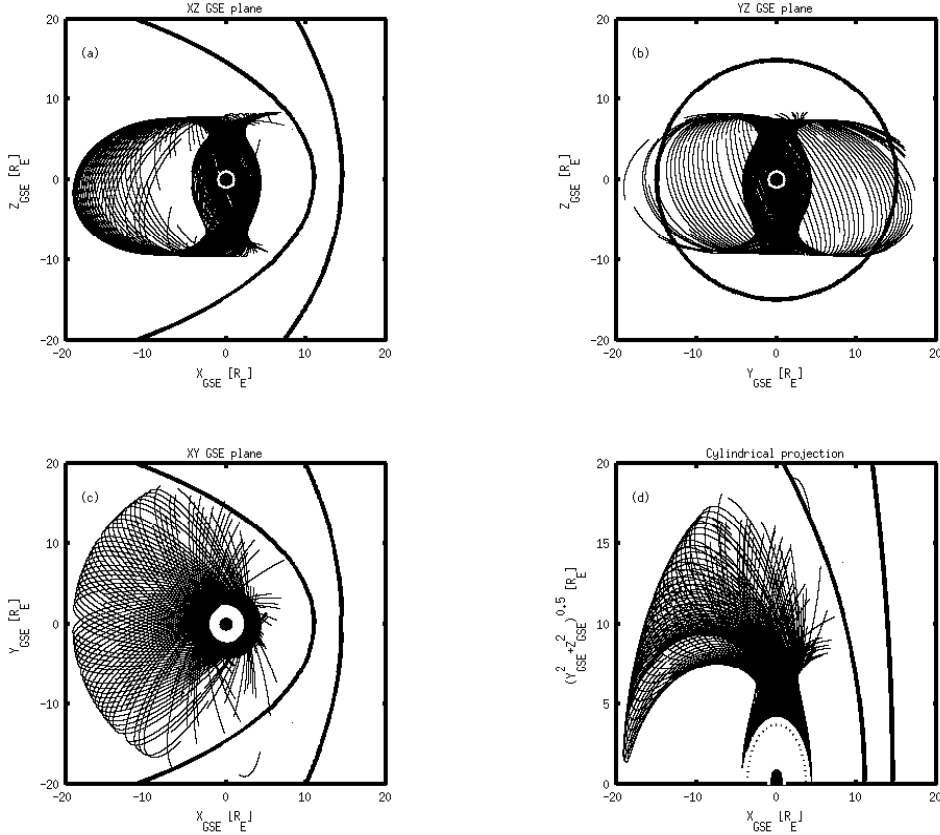
749 **Figure 8.** GUMICS-4 simulation results (black) and Cluster SC3 magnetic field, ion plasma  
 750 moments (red) and electron density calculated from spacecraft potential (blue) from February 11,  
 751 2002 from 2:30 to 9:00 (UT) in the magnetosheath in GSE system (a) Magnetic field Z compo-  
 752 nent. (b) Solar wind velocity X component (c) Solar wind density.



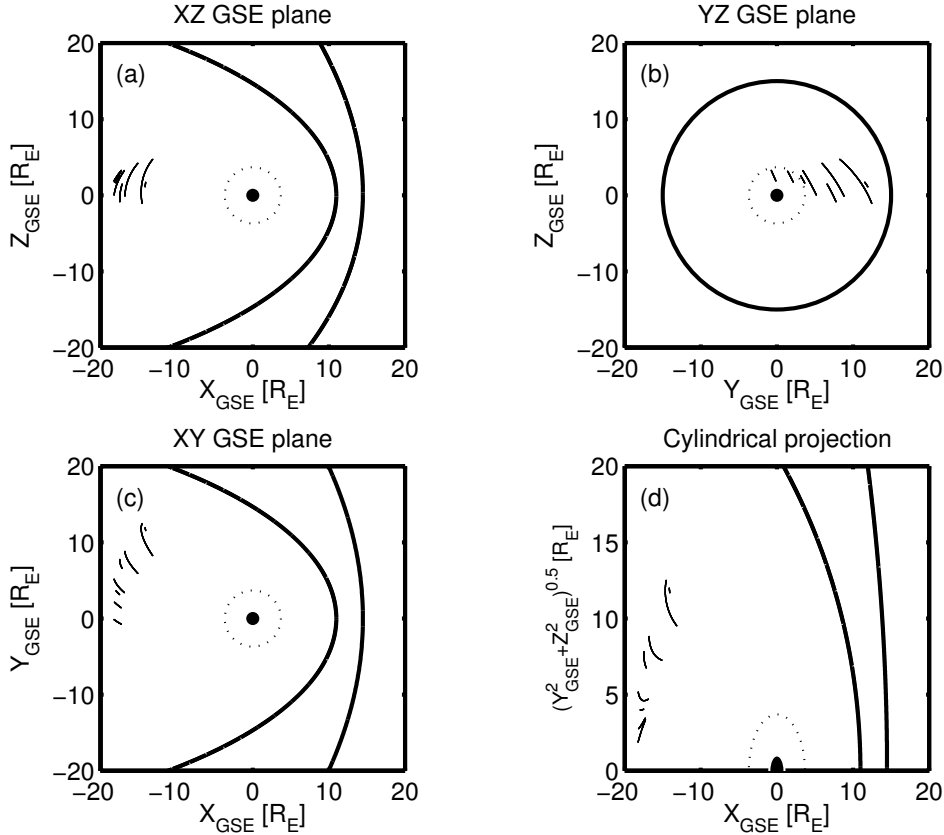
753 **Figure 9.** Scattered plots of the Cluster SC3 and GUMICS-4 simulations for all intervals in  
 754 the magnetosheath in GSE system. The dashed line is the  $y=x$  line. (a) Magnetic field Z com-  
 755 ponent. (b) Solar wind velocity X component. (c) Solar wind density measured by the CIS HIA  
 756 instrument (red) and calculated from the spacecraft potential (blue).



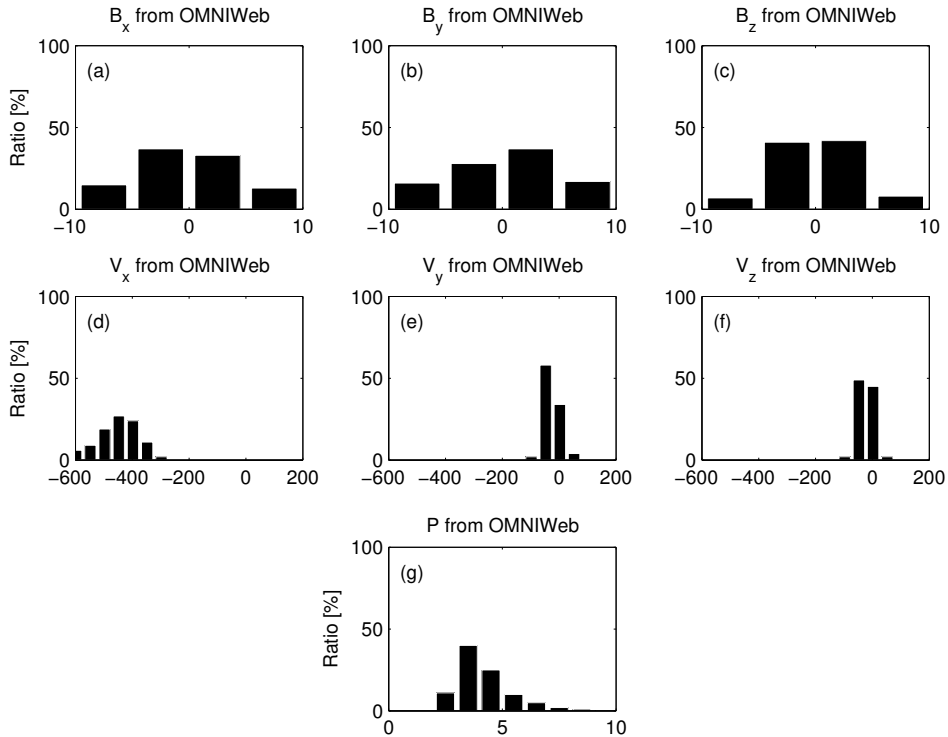
757      **Figure 10.** The distributions of the correlation coefficients (a, c, e, g) of the magnetic field Z  
 758      component ( $B_z$ ) in GSE system, solar wind velocity X component ( $V_x$ ) in GSE system, the solar  
 759      wind density measured by the CIS HIA ( $n_{CIS}$ ) instrument and calculated from the spacecraft  
 760      potential ( $n_{EFW}$ ), respectively, for all intervals in the magnetosheath. The distributions of the  
 761      time shifts (b, d, f, h) of the  $B_z$ , the  $V_x$ , the  $n_{CIS}$  and the  $n_{EFW}$ , respectively, for all intervals  
 762      in the magnetosheath.



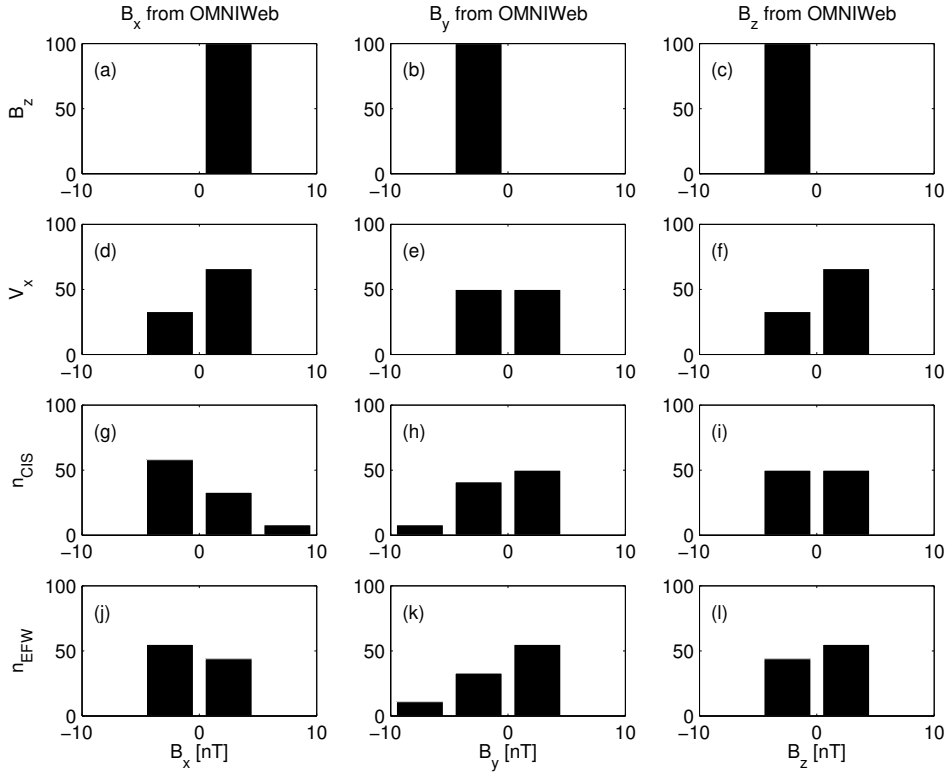
763 **Figure 11.** Cluster SC3 orbit in the magnetosphere in GSE system for all intervals (see Ta-  
 764 ble 3). (a) XZ (b) YZ (c) XY (d) Cylindrical projection. Average bow-shock and magnetopause  
 765 positions are drawn on all plots using solid line [Peredo *et al.*, 1995; Tsyganenko, 1995, respec-  
 766 tively]. The black dots at  $3.7 R_E$  show the boundary of the GUMICS-4 inner magnetospheric  
 767 domain. The black circle in the origo of all plots shows the size of the Earth.



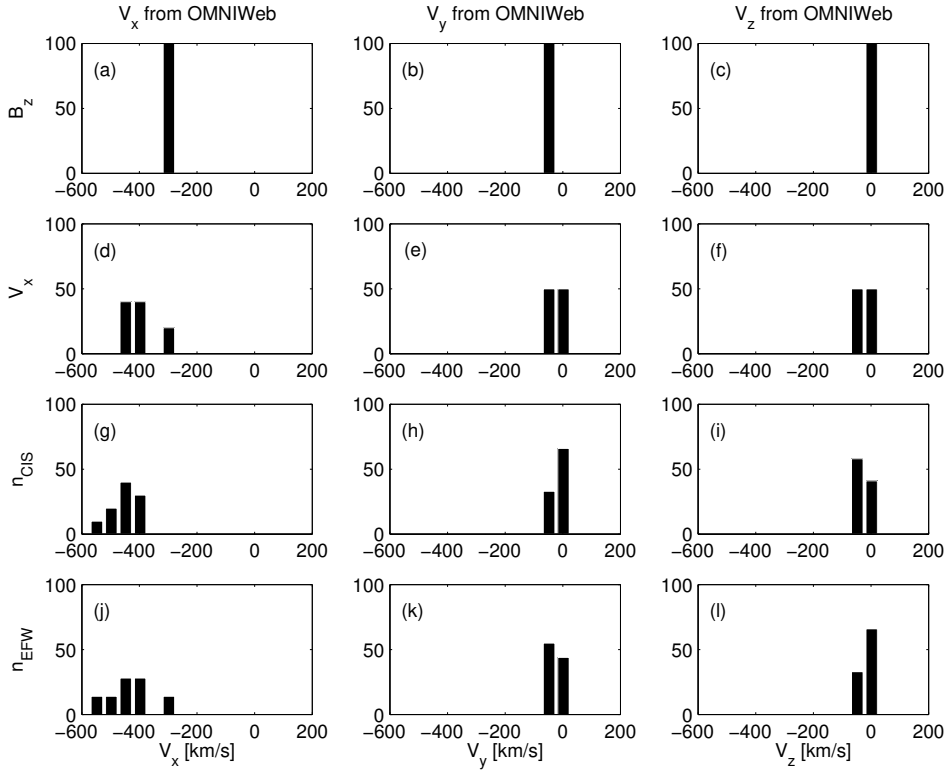
768 **Figure 12.** Cluster SC3 orbit in the tail in GSE system for all intervals (see Table 6). (a)  
 769 (b) (c) (d) Cylindrical projection. Average bow-shock and magnetopause positions  
 770 are drawn on all plots using solid line [Perego *et al.*, 1995; Tsyganenko, 1995, respectively]. The  
 771 black dots at  $3.7 R_E$  show the boundary of the GUMICS–4 inner magnetospheric domain. The  
 772 black circle in the origo of all plots shows the size of the Earth.



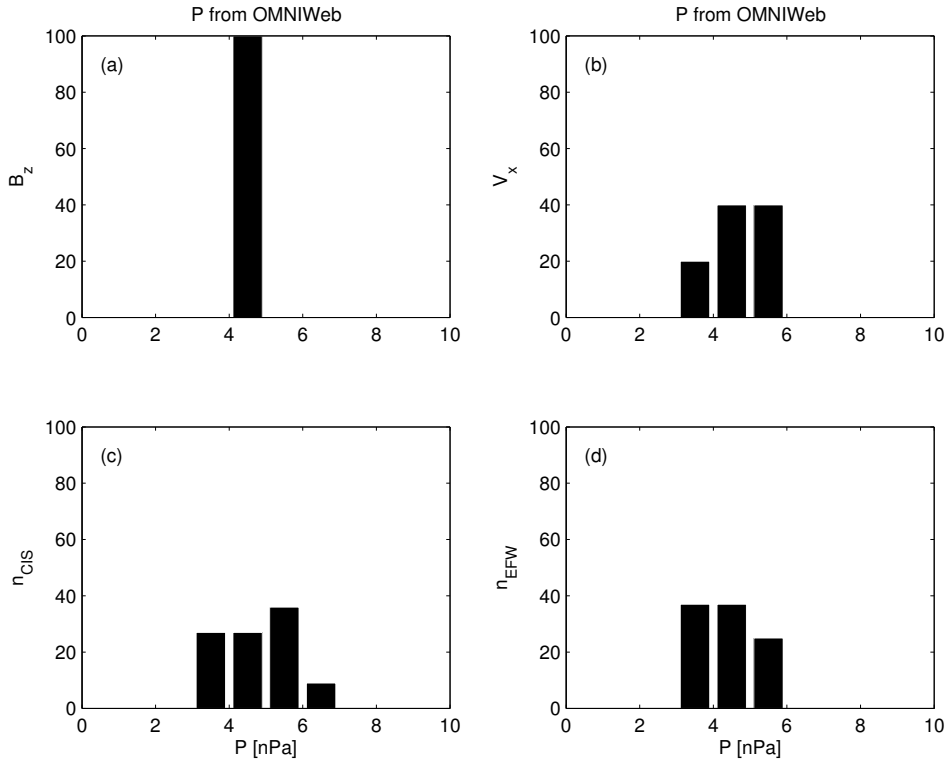
773      **Figure 13.** (a, b, c) The distributions of the OMNI solar wind magnetic field ( $B_x$ ,  $B_y$ ,  $B_z$ )  
 774      components, (d, e, f) the OMNI solar wind velocity ( $V_x$ ,  $V_y$ ,  $V_z$ ) components and (g) the solar  
 775      wind dynamic pressure during the 1-year run from January 29, 2002 to February 2, 2003 in GSE  
 776      reference frame, respectively. The relative values are given on the vertical axis of all plots in  
 777      percentage.



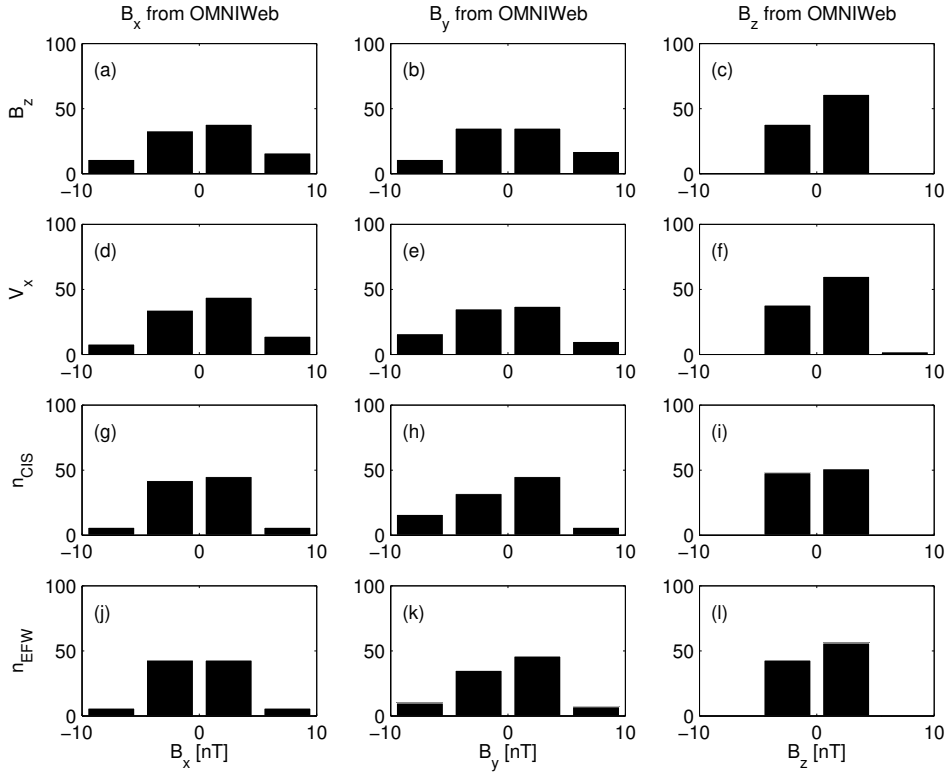
778 **Figure 14.** The distributions of the  $B_x$ , the  $B_y$  and the  $B_z$  OMNI solar wind magnetic field  
 779 components when the agreement of the Cluster SC3 measurements and the GUMICS–4 simu-  
 780 lations are poor in the solar wind (see Table 4). The  $B_z$ , the  $V_x$ , the  $n_{\text{CIS}}$  and the  $n_{\text{EFW}}$  are  
 781 the magnetic field GSE Z component, the plasma ion velocity X GSE component, the solar wind  
 782 density measured by the CIS HIA instrument and the calculated from the EFW spacecraft po-  
 783 tential, respectively. (a, b, c) Distribution of OMNI  $B_x$ ,  $B_y$ ,  $B_z$  when the agreement of  $B_z$  is  
 784 poor. (d, e, f) Distribution of OMNI  $B_x$ ,  $B_y$ ,  $B_z$  when the agreement of  $V_x$  is poor. (g, h, i)  
 785 Distribution of OMNI  $B_x$ ,  $B_y$ ,  $B_z$  when the agreement of  $n_{\text{CIS}}$  is poor. (j, k, l) Distribution of  
 786 OMNI  $B_x$ ,  $B_y$ ,  $B_z$  when the agreement of  $n_{\text{EFW}}$  is poor. The values are in percentage unit in  
 787 the distributions.



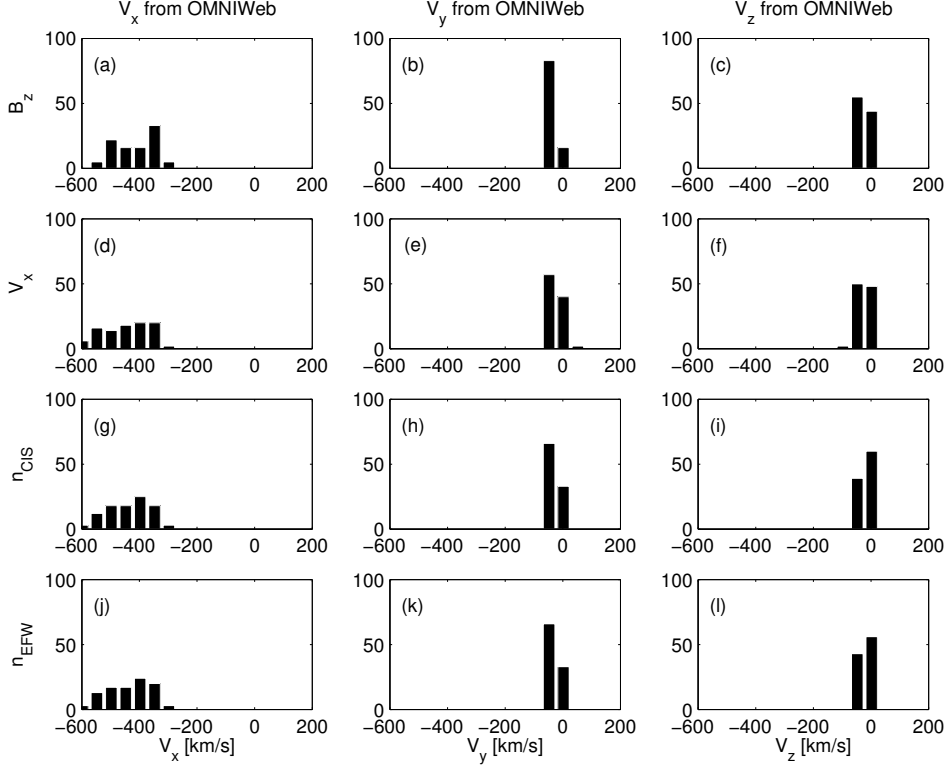
788 **Figure 15.** The distributions of the  $V_x$ , the  $V_y$  and the  $V_z$  OMNI solar wind magnetic field  
 789 components when the agreement of the Cluster SC3 measurements and the GUMICS–4 simu-  
 790 lations are poor in the solar wind (see Table 4). The  $B_z$ , the  $V_x$ , the  $n_{CIS}$  and the  $n_{EFW}$  are  
 791 the magnetic field GSE Z component, the plasma ion velocity X GSE component, the solar wind  
 792 density measured by the CIS HIA instrument and the calculated from the EFW spacecraft po-  
 793 tential, respectively. (a, b, c) Distribution of OMNI  $V_x$ ,  $V_y$ ,  $V_z$  when the agreement of  $B_z$  is poor.  
 794 (d, e, f) Distribution of OMNI  $V_x$ ,  $V_y$ ,  $V_z$  when the agreement of  $V_x$  is poor. (g, h, i) Distribution  
 795 of OMNI  $V_x$ ,  $V_y$ ,  $V_z$  when the agreement of  $n_{CIS}$  is poor. (j, k, l) Distribution of OMNI  $V_x$ ,  $V_y$ ,  
 796  $V_z$  when the agreement of  $n_{EFW}$  is poor. The values are in percentage unit in the distributions.



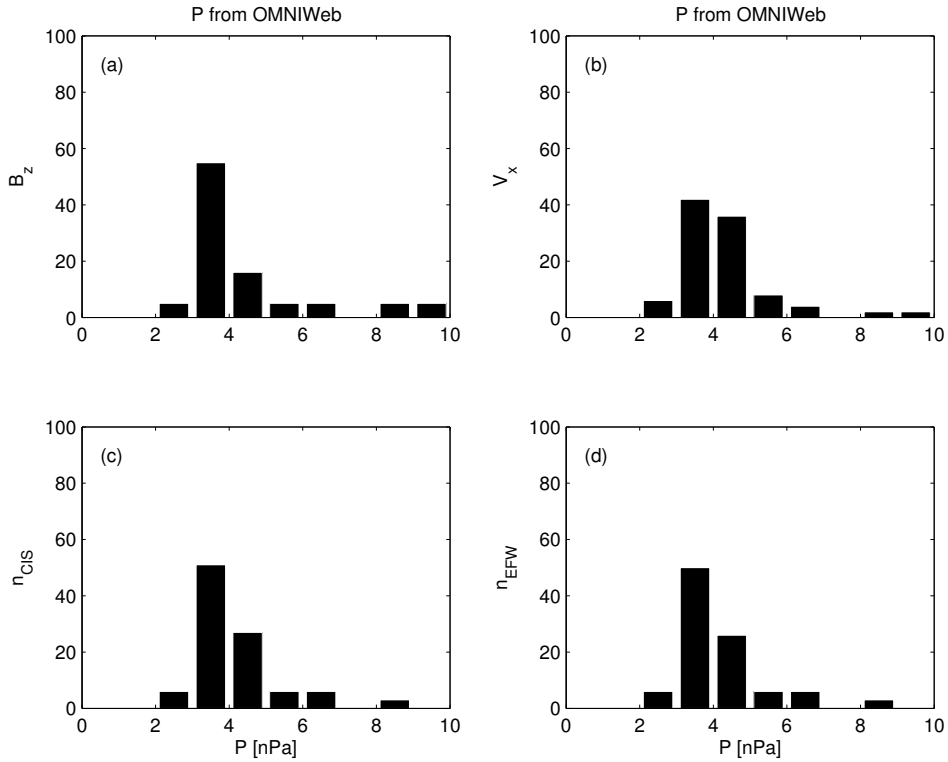
797 **Figure 16.** The distributions of the  $P$  solar wind dynamic pressure calculated from OMNI  
 798 parameters when the agreement of the Cluster SC3 measurements and the GUMICS–4 simula-  
 799 tions are poor in the solar wind (see Table 4). The  $B_z$ ,  $V_x$ ,  $n_{CIS}$  and  $n_{EFW}$  are the magnetic  
 800 field GSE Z component, the velocity X GSE component, the solar wind density measured by the  
 801 CIS HIA instrument and calculated from the EFW spacecraft potential, respectively. (a, b, c, d)  
 802 The distribution of the  $P$  calculated from OMNI data when the agreement of the  $B_z$ , the  $V_x$ , the  
 803  $n_{CIS}$  or the  $n_{EFW}$  are poor. The values are in percentage unit in the distributions.



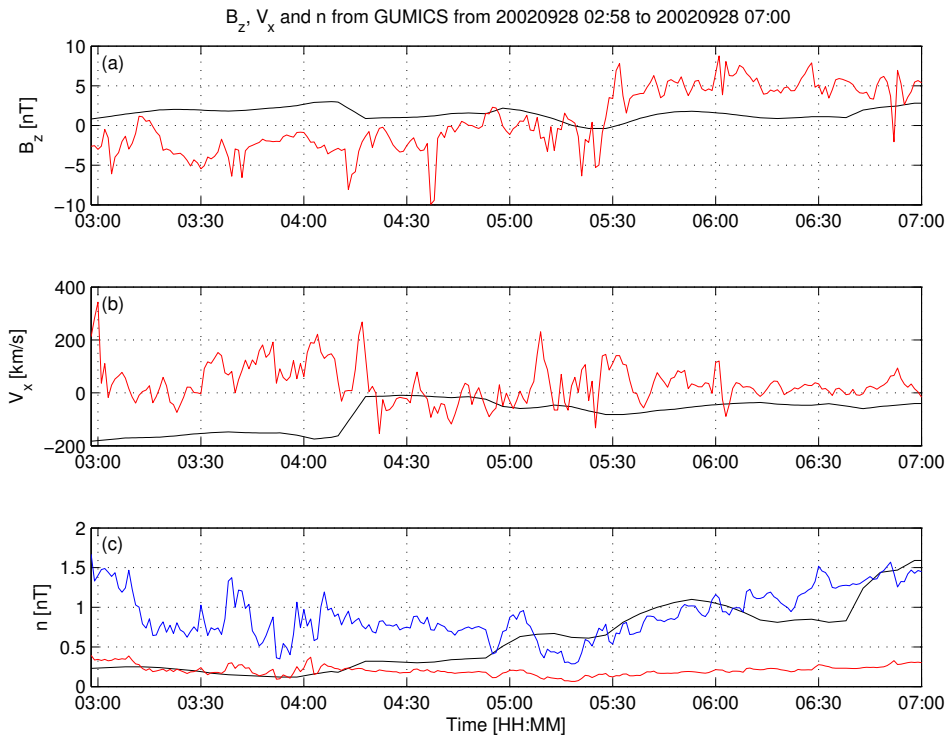
804 **Figure 17.** The distributions of the  $B_x$ , the  $B_y$  and the  $B_z$  OMNI solar wind magnetic field  
 805 components when the agreement of the Cluster SC3 measurements and the GUMICS–4 simu-  
 806 lations are poor in the magnetosheath (see Table 5). The  $B_z$ , the  $V_x$ , the  $n_{CIS}$  and the  $n_{EFW}$   
 807 are the magnetic field GSE Z component, the plasma ion velocity X GSE component, the solar  
 808 wind density measured by the CIS HIA instrument and the calculated from the EFW space-  
 809 craft potential, respectively. (a, b, c) Distribution of OMNI  $B_x$ ,  $B_y$ ,  $B_z$  when the agreement of  $B_z$   
 810 is poor. (d, e, f) Distribution of OMNI  $B_x$ ,  $B_y$ ,  $B_z$  when the agreement of  $V_x$  is poor. (g, h, i)  
 811 Distribution of OMNI  $B_x$ ,  $B_y$ ,  $B_z$  when the agreement of  $n_{CIS}$  is poor. (j, k, l) Distribution of  
 812 OMNI  $B_x$ ,  $B_y$ ,  $B_z$  when the agreement of  $n_{EFW}$  is poor. The values are in percentage unit in  
 813 the distributions.



814      **Figure 18.** The distributions of the  $V_x$ , the  $V_y$  and the  $V_z$  OMNI solar wind magnetic field  
 815      components when the agreement of the Cluster SC3 measurements and the GUMICS–4 simula-  
 816      tions are poor in the magnetosheath (see Table 5). The  $B_z$ , the  $V_x$ , the  $n_{CIS}$  and the  $n_{EFW}$  are  
 817      the magnetic field GSE Z component, the plasma ion velocity X GSE component, the solar wind  
 818      density measured by the CIS HIA instrument and the calculated from the EFW spacecraft po-  
 819      tential, respectively. (a, b, c) Distribution of OMNI  $V_x$ ,  $V_y$ ,  $V_z$  when the agreement of  $B_z$  is poor.  
 820      (d, e, f) Distribution of OMNI  $V_x$ ,  $V_y$ ,  $V_z$  when the agreement of  $V_x$  is poor. (g, h, i) Distribution  
 821      of OMNI  $V_x$ ,  $V_y$ ,  $V_z$  when the agreement of  $n_{CIS}$  is poor. (j, k, l) Distribution of OMNI  $V_x$ ,  $V_y$ ,  
 822       $V_z$  when the agreement of  $n_{EFW}$  is poor. The values are in percentage unit in the distributions.



823      **Figure 19.** The distributions of the  $P$  solar wind dynamic pressure calculated from OMNI pa-  
 824      rameters when the agreement of the Cluster SC3 measurements and the GUMICS-4 simulations  
 825      are poor in the magnetosheath (see Table 5). The  $B_z$ ,  $V_x$ ,  $n_{CIS}$  and  $n_{EFW}$  are the magnetic  
 826      field GSE Z component, the velocity X GSE component, the solar wind density measured by the  
 827      CIS HIA instrument and calculated from the EFW spacecraft potential, respectively. (a, b, c, d)  
 828      The distribution of the  $P$  calculated from OMNI data when the agreement of the  $B_z$ , the  $V_x$ , the  
 829       $n_{CIS}$  or the  $n_{EFW}$  are poor. The values are in percentage unit in the distributions.



830      **Figure 20.** GUMICS-4 simulation results (black) and Cluster SC3 magnetic field, ion plasma  
 831      moments (red) and electron density calculated from spacecraft potential (blue) from September  
 832      28, 2002 from 2:58 to 7:00 (UT) in the tail in GSE system. (a) Magnetic field Z component. (b)  
 833      Solar wind velocity X component (c) Solar wind density.

Start/End	$C_{B_z}$	$\delta t_{B_z}$	$C_{V_x}$	$\delta t_{V_x}$	$C_{n_{CIS}}$	$\delta t_{n_{CIS}}$	$C_{n_{EFW}}$	$\delta t_{n_{EFW}}$
	[min]		[min]		[min]		[min]	
20020201 20:00/0203 04:00	0.96	2	1.00	13	0.96	3	0.98	3
20020211 13:00/0212 12:00	0.82	2	1.00	0	0.99	18	0.99	18
20020218 09:00/0219 02:00	0.93	0	1.00	-3	0.94	-3	0.97	-3
20020219 06:30/0219 15:00	0.93	1	1.00	0	0.99	-60	1.00	-52
20020220 18:30/0222 00:00	0.87	4	1.00	4	0.93	-21	0.98	3
20020318 17:30/0319 02:30	0.89	1	1.00	21	0.98	50	0.99	5
20020412 20:30/0413 02:00	0.90	4	0.99	-54	0.94	60	0.98	12
20021227 12:00/1228 03:00	0.75	4	1.00	-3	0.99	-26	0.99	21
20021229 20:00/1230 16:00	0.68	1	1.00	1	0.99	-30	0.98	41
20030106 06:00/0106 19:00	0.79	4	1.00	6	0.99	4	0.99	-60
20030108 07:00/0109 03:30	0.55	10	1.00	41	0.99	10	0.97	-55
20030113 08:30/0113 18:00	0.91	3	1.00	5	1.00	3	0.97	-1
20030120 07:30/0120 13:00	0.82	2	1.00	9	1.00	-6	1.00	-3
20030122 12:00/0123 14:00	0.81	2	1.00	3	0.99	3	0.92	-60
20030124 18:00/0126 00:00	0.73	3	1.00	0	0.99	-60	0.99	60
20030127 16:00/0128 06:00	0.88	-1	1.00	-3	0.95	1	0.88	11
20030129 12:00/0130 18:00	0.90	2	1.00	4	0.94	-59	0.98	1

**Table 1.** The studied solar wind intervals. The correlation coefficients ( $C_{B_z}$ ,  $C_{V_x}$ ,  $C_{n_{CIS}}$ ,  $C_{n_{EFW}}$ ) and time shift ( $\delta t_{V_x}$ ,  $\delta t_{n_{CIS}}$ ,  $\delta t_{n_{EFW}}$ ) in minutes of the magnetic field GSE Z component ( $B_z$ ), solar wind velocity X component ( $V_x$ ), CIS and EFW densities ( $n_{CIS}$ ,  $n_{EFW}$ ).

Table 2: The studied magnetosheath intervals. The correlation coefficients ( $C_{B_z}$ ,  $C_{V_x}$ ,  $C_{n_{CIS}}$ ,  $C_{n_{EFW}}$ ) and time shift ( $\delta t_{V_x}$ ,  $\delta t_{n_{CIS}}$ ,  $\delta t_{n_{EFW}}$ ) in minutes of the magnetic field GSE Z component ( $B_z$ ), solar wind velocity X component ( $V_x$ ), CIS and EFW densities ( $n_{CIS}$ ,  $n_{EFW}$ ). In the empty slots the correlation calculation gives invalid result.

Start/End	$C_{B_z}$	$\delta t_{B_z}$	$C_{V_x}$	$\delta t_{V_x}$	$C_{n_{CIS}}$	$\delta t_{n_{CIS}}$	$C_{n_{EFW}}$	$\delta t_{n_{EFW}}$
		[min]		[min]		[min]		[min]
20020201 13:30/0201 18:30	0.91	1	0.98	56	0.99	60	0.976	60
20020208 18:15/0209 00:00	0.73	2	0.95	60	0.98	-52	0.98	-54
20020211 02:30/0211 09:00	0.79	0	0.99	-20	0.99	-1	0.99	1
20020212 16:30/0212 21:00	0.80	3	0.99	54	0.99	31	0.99	30
20020219 17:30/0219 23:00	0.76	4	0.98	37	0.99	7	0.99	6
20020222 23:00/0223 06:30	0.64	0	0.97	-60	0.99	-47	0.98	-48
20020227 16:30/0227 23:15	0.48	59	0.98	-31	0.99	-39	1.00	-12
20020310 18:30/0311 00:30	0.97	3	0.98	19	0.99	8	0.99	-2
20020311 14:00/0311 19:00	0.86	5	0.97	36	0.99	-3	0.99	-40
20020406 19:00/0407 01:15	0.76	2	0.96	-60	0.98	-55	0.98	-56
20020410 17:30/0410 23:00	0.89	6	0.99	-50	0.99	3	1.00	5
20020411 11:30/0411 16:30	0.82	4	0.99	39	0.99	3	0.99	3
20020418 18:30/0418 22:45	0.92	60	0.99	-60	0.99	60	0.98	60
20020421 04:30/0421 07:45	0.96	47	0.99	-60	1.00	-60	1.00	-60
20020422 11:45/0422 15:45	0.73	-5	0.98	-17	0.99	-15	0.98	-16
20020423 08:30/0423 12:30	0.93	31	0.99	3	0.99	16	0.99	16
20020430 12:30/0430 17:00	0.79	59	0.98	22	0.98	-18		
20020505 07:00/0505 11:15	0.71	59	0.99	-58	0.98	-60		
20020506 19:15/0507 00:15	0.84	-27	0.98	-60	0.97	-37		
20020507 17:30/0507 23:00	0.93	2	0.98	-30	0.99	-49		
20020514 22:45/0515 03:00	0.79	49	0.99	35	0.99	38	0.99	43
20020517 07:00/0517 12:15	0.74	-5	1.00	-5	0.99	-4	0.99	-3
20020518 13:30/0518 19:30	0.70	1	0.99	9	0.97	-1	0.97	-1

*Continued on next page*

Table 2 – *Continued from previous page*

Start/End	$C_{B_z}$	$\delta t_{B_z}$	$C_{V_x}$	$\delta t_{V_x}$	$C_{n_{CIS}}$	$\delta t_{n_{CIS}}$	$C_{n_{EFW}}$	$\delta t_{n_{EFW}}$
		[min]		[min]		[min]		[min]
20020519 20:00/0520 03:30	0.98	2	1.00	-9	0.99	-5	0.99	-50
20020520 10:45/0520 20:15	0.77	1	0.99	-3	0.95	-1	0.99	-1
20020522 02:00/0522 08:45	0.49	52	0.99	4	0.99	12	0.99	22
20020527 02:15/0527 17:15	0.79	-3	0.99	-3	0.98	0	0.98	0
20020530 05:00/0530 10:30	0.29	3	1.00	-38	0.99	3	0.99	3
20020601 19:30/0602 01:00	0.68	-2	1.00	18	0.99	-6	0.99	-7
20020602 21:45/0603 17:45	0.62	-5	0.99	-1	0.98	2	0.99	2
20020605 10:30/0606 06:00	0.18	0	1.00	-7	0.97	10	0.98	9
20020607 18:00/0607 22:00	0.92	-35	1.00	-36	0.99	16	0.99	16
20020608 01:15/0608 18:15	0.53	-4	0.99	-39	0.96	-6	0.97	-6
20020610 01:30/0610 09:30	0.76	5	0.99	8	0.99	-5	0.99	-7
20020610 11:00/0611 01:00	0.87	-4	0.99	-33	0.98	23	0.99	6
20020612 18:30/0613 06:15	0.44	-2	0.99	-7	0.97	4	0.97	-32
20020615 07:00/0615 23:30			1.00	47	0.98	-3	0.98	-3
20020617 05:00/0618 03:45	0.76	4	1.00	28	0.98	10	0.98	8
20020620 04:00/0620 11:00	0.61	-8	0.99	-6	0.97	12	0.98	4
20020622 14:30/0622 18:00	0.98	55	1.00	35	0.99	16	1.00	16
20021201 04:15/1202 07:45	0.38	1	1.00	2	0.99	6	0.99	6
20021203 15:30/1204 19:30	0.67	1	0.99	60	0.98	59	0.98	59
20021207 00:30/1207 07:45	0.49	37	0.98	-56	0.99	-19	0.99	-4
20021208 09:30/1209 08:00	0.69	2	0.98	-35	0.97	6	0.98	4
20021212 23:30/1213 14:30	0.51	5	1.00	36	0.99	-3	0.81	-56
20021213 21:15/1214 09:30	0.93	5	0.99	-35	0.99	-13	0.99	-47
20021215 12:45/1216 18:00	0.76	2	0.99	-60	0.94	-60	0.98	31
20021217 16:30/1218 01:45	0.99	2	1.00	-54	0.99	3	0.99	3
20021220 01:30/1220 06:15	0.92	0	1.00	60	0.99	2	0.99	3
20021223 02:15/1223 13:00	0.91	1	0.97	49	0.93	49	0.99	-14
20021223 14:00/1223 22:30	0.84	1	0.99	-2	0.99	-1	1.00	-3
20021224 19:00/1225 01:45	0.94	0	1.00	-44	0.99	26	0.99	27

*Continued on next page*

Table 2 – *Continued from previous page*

Start/End	$C_{B_z}$	$\delta t_{B_z}$	$C_{V_x}$	$\delta t_{V_x}$	$C_{n_{CIS}}$	$\delta t_{n_{CIS}}$	$C_{n_{EFW}}$	$\delta t_{n_{EFW}}$
		[min]		[min]		[min]		[min]
20021225 23:45/1226 07:15	0.96	7	1.00	-17	0.99	56	0.99	55
20021226 23:00/1227 09:45	0.79	2	1.00	2	0.98	4	0.99	3
20021229 11:45/1229 17:00	0.60	2	1.00	-60	0.98	-19	0.98	50
20021230 17:45/1231 01:00	0.69	1	0.98	52	0.98	60	0.98	22
20021231 23:00/0101 05:15	0.89	2	0.99	15	0.99	-54	1.00	-58
20030105 14:00/0105 21:00	0.69	0	0.99	1	0.98	-60	0.99	-60
20030106 23:15/0107 03:00	0.52	9	0.98	60	0.99	56	1.00	-60
20030109 08:45/0109 16:15			0.91	-56	0.98	-13	0.98	-26
20030110 07:15/0110 15:15	0.94	1	0.99	-7	0.99	1	0.98	5
20030111 08:15/0111 22:30	0.84	0	0.99	-59	0.94	-15	0.94	8
20030112 17:30/0113 00:15	0.98	0	1.00	-52	0.99	39	0.99	51
20030114 00:30/0114 08:30	0.84	-1	0.99	-60	0.98	23	0.98	8
20030116 10:15/0116 17:45	0.62	60	0.93	52	0.99	60	0.99	30
20030117 09:30/0117 13:30	0.68	-3	1.00	8	1.00	-31	0.99	-33
20030118 23:30/0119 03:45	0.93	3	1.00	-12	1.00	7	0.99	7
20030119 21:00/0120 01:00	0.94	3	1.00	5	1.00	38	1.00	19
20030121 06:30/0121 11:30	0.82	-15	0.96	47	0.98	7	0.99	-39
20030122 04:45/0122 09:30	0.69	-2	1.00	10	0.99	-9	0.99	-5
20030126 01:45/0126 06:30	0.85	3	0.99	-15	0.99	-50	0.99	23
20030127 08:15/0127 13:00	1.00	9	1.00	-60	0.98	0	0.99	1
20030128 12:30/0128 17:15	0.77	60	0.99	-24	0.99	-6	0.988	20
20030130 19:45/0131 00:15	0.98	2	0.99	51	0.99	25	0.99	9

Table 3: The studied magnetosphere intervals (UT).

Start/End
20020213 23:00/0214 01:30
20020217 18:30/0218 02:00
20020220 00:45/0220 12:00
20020222 11:15/0222 20:15
20020225 02:15/0225 08:30
20020227 06:00/0227 12:00
20020302 00:00/0302 03:15
20020306 10:00/0306 18:30
20020308 17:30/0309 06:00
20020311 02:15/0311 12:00
20020313 11:15/0314 00:15
20020316 04:45/0316 08:00
20020318 09:00/0318 14:45
20020320 20:30/0320 23:55
20020323 04:00/0323 09:45
20020327 23:45/0328 06:15
20020330 07:15/0330 12:45
20020401 19:30/0401 22:00
20020406 09:30/0406 18:00
20020408 15:00/0409 00:00
20020410 23:30/0411 09:45
20020413 08:30/0413 19:00
20020416 18:00/0417 04:30
20020418 06:00/0418 12:00
20020420 15:00/0420 23:00
20020422 20:00/0423 07:00
20020425 08:30/0425 18:00
20020430 04:40/0430 12:00
20020504 14:30/0504 16:45

*Continued on next page*

Table 3 – *Continued from previous page*

Start/End
20020505 02:30/0505 07:00
20020507 01:30/0507 15:45
20020508 11:00/0510 04:15
20020512 02:45/0512 09:30
20020514 10:30/0514 12:45
20020519 00:30/0519 19:30
20020521 01:30/0521 22:00
20020523 23:30/0524 02:00
20020524 19:00/0525 08:15
20020526 07:30/0526 10:30
20020528 20:00/0529 05:00
20020531 02:15/0531 13:30
20020602 04:30/0602 07:30
20020602 12:00/0602 21:30
20020604 08:30/0605 07:00
20020606 14:30/0607 16:30
20020609 06:00/0609 20:00
20020611 11:00/0612 13:00
20020614 01:00/0614 16:00
20020616 08:00/0616 18:00
20020620 13:30/0622 01:00
20020623 13:00/0623 17:00
20020624 04:00/0624 10:15
20020630 17:45/0701 15:00
20020701 21:00/0703 10:30
20020703 23:00/0706 03:15
20020707 01:00/0708 23:00
20020710 11:30/0714 03:30
20020714 15:45/0715 15:30
20020716 23:30/0717 16:00

*Continued on next page*

Table 3 – *Continued from previous page*

Start/End
20020718 05:45/0722 11:00
20020722 23:45/0728 01:00
20020728 02:00/0804 03:45
20020804 04:45/0811 06:15
20020811 07:30/0816 01:00
20020816 15:30/0818 09:00
20020818 10:00/0825 11:30
20020825 13:00/0901 14:15
20020901 17:15/0903 23:30
20020905 02:15/0906 16:30
20020907 10:30/0908 17:00
20020908 18:00/0915 19:30
20020915 21:00/0922 22:30
20020923 00:00/0923 23:30
20020924 03:30/0928 22:45
20020928 23:30/0930 01:00
20020930 02:15/1006 17:00
20021006 17:45/1007 03:30
20021007 05:00/1007 17:30
20021008 07:30/1010 22:00
20021010 22:30/1012 22:30
20021012 23:00/1014 06:30
20021014 09:00/1016 04:00
20021016 14:00/1019 00:15
20021019 01:30/1019 22:00
20021021 04:00/1022 19:30
20021022 22:30/1026 02:30
20021026 04:00/1029 20:15
20021030 01:30/1102 08:00
20021102 22:00/1104 22:00

*Continued on next page*

Table 3 – *Continued from previous page*

Start/End
20021106 00:00/1107 18:00
20021108 02:00/1109 18:45
20021111 00:00/1112 01:30
20021113 03:45/1114 14:15
20021115 20:30/1116 23:00
20021118 01:00/1118 23:30
20021120 17:00/1121 06:00
20021122 21:30/1124 01:00
20021125 04:00/1126 08:30
20021127 20:00/1128 18:30
20021130 04:00/1201 01:30
20021202 14:30/1203 09:00
20021204 22:00/1205 19:30
20021207 09:00/1207 16:30
20021207 18:00/1207 22:00
20021209 16:30/1210 14:30
20021212 13:45/1212 21:30
20021214 13:30/1214 20:00
20021214 21:00/1215 07:30
20021216 21:00/1217 15:00
20021219 08:00/1219 19:30
20021221 15:45/1221 23:15
20021222 00:30/1222 08:45
20021224 02:30/1224 14:00
20021226 10:00/1226 19:00
20021228 19:30/1229 02:30
20021229 04:00/1229 10:00
20021231 05:00/1231 18:45
20030102 12:30/0102 20:45
20030104 20:45/0105 06:00

*Continued on next page*

Table 3 – *Continued from previous page*

Start/End
20030105 07:00/0105 13:30
20030107 05:45/0107 21:00
20030109 17:00/0110 00:45
20030112 00:00/0112 09:15
20030112 10:30/0112 16:00
20030114 11:00/0114 20:00
20030116 20:30/0116 22:45
20030119 04:30/0119 09:30
20030119 14:00/0119 17:00
20030121 13:30/0121 21:30
20030126 07:30/0126 15:45
20030128 17:45/0129 08:15
20030131 01:30/0131 11:45

Start/End	OMNI			Cluster SC3			
	$B_z$ [nT]	$V_x$ [km/s]	P [cm $^{-3}$ ]	$B_z$	$V_x$	$n_{CIS}$	$n_{EFW}$
20020201 20:00/0203 04:00	-1.25	-373.52	4.08	y	y	n	y
20020211 13:00/0212 12:00	0.03	-533.11	2.18	y	y	y	y
20020218 09:00/0219 02:00	2.56	-362.41	3.46	y	n	n	y
20020219 06:30/0219 15:00	3.55	-401.63	1.25	y	y	n	n
20020220 18:30/0222 00:00	1.95	-440.18	1.96	y	y	n	y
20020318 17:30/0319 02:30	3.79	-429.30	15.34	y	n	n	n
20020412 20:30/0413 02:00	-1.81	-420.35	3.24	y	n	n	y
20021227 12:00/1228 03:00	0.09	-714.40	2.72	y	n	n	y
20021229 20:00/1230 16:00	-0.37	-526.40	2.26	y	y	n	n
20030106 06:00/0106 19:00	2.25	-399.91	1.50	y	n	n	n
20030108 07:00/0109 03:30	-0.58	-280.80	2.97	n	n	y	n
20030113 08:30/0113 18:00	0.68	-397.83	1.72	y	y	y	n
20030120 07:30/0120 13:00	2.16	-630.69	2.43	y	y	y	y
20030122 12:00/0123 14:00	0.13	-608.96	3.41	y	y	y	n
20030124 18:00/0126 00:00	-0.71	-739.68	2.87	y	y	n	n
20030127 16:00/0128 06:00	-0.92	-451.84	3.12	y	y	n	n
20030129 12:00/0130 18:00	-3.09	-450.00	3.96	y	y	n	y

839 **Table 4.** The average OMNI input parameters in the solar wind and the good/bad agreement  
 840 of the GUMICS-4 simulations to the Cluster  $B_z$  magnetic field component, the  $V_x$  solar wind  
 841 speed component, the  $n_{CIS}$  solar wind density measured by the Cluster CIS HIA instrument and  
 842 the  $n_{EFW}$  solar wind density calculated from the spacecraft potential measured by the Cluster  
 843 EFW instrument in the solar wind.

Table 5: The average OMNI input parameters in the solar wind and the good/bad agreement of the GUMICS–4 simulations to the Cluster  $B_z$  magnetic field component, the  $V_x$  solar wind speed component, the  $n_{CIS}$  solar wind density measured by the Cluster CIS HIA instrument and the  $n_{EFW}$  solar wind density calculated from the spacecraft potential measured by the Cluster EFW instrument in the magnetosheath.

Start/End	OMNI			Cluster SC3			
	$B_z$	$V_x$	P	$B_z$	$V_x$	$n_{CIS}$	$n_{EFW}$
	[nT]	[km/s]	[cm $^{-3}$ ]				
20020201 13:30/0201 18:30	0.19	-342.87	4.62	y	n	n	n
20020208 18:15/0209 00:00	-0.48	-508.16	1.61	y	n	n	n
20020211 02:30/0211 09:00	-1.85	-425.67	1.78	y	y	y	y
20020212 16:30/0212 21:00	2.98	-509.22	2.34	y	n	n	n
20020219 17:30/0219 23:00	1.46	-431.50	1.46	y	y	y	y
20020222 23:00/0223 06:30	0.86	-391.22	1.14	y	n	n	n
20020227 16:30/0227 23:15	1.89	-343.13	1.52	n	n	n	n
20020310 18:30/0311 00:30	-2.81	-379.46	1.78	y	y	y	y
20020311 14:00/0311 19:00	1.63	-371.43	2.68	n	n	n	n
20020406 19:00/0407 01:15	-2.71	-333.13	0.93	y	n	n	n
20020410 17:30/0410 23:00	0.31	-312.43	4.42	n	n	y	y
20020411 11:30/0411 16:30	-1.50	-494.02	4.25	y	y	n	n
20020418 18:30/0418 22:45	-0.92	-450.82	0.30	n	n	n	n
20020421 04:30/0421 07:45	0.40	-455.69	1.37	n	n	n	n
20020422 11:45/0422 15:45	0.25	-419.98	1.14	n	n	y	y
20020423 08:30/0423 12:30	2.77	-507.99	6.82	n	n	n	n
20020430 12:30/0430 17:00	2.15	-479.51	3.02	n	n	n	n
20020505 07:00/0505 11:15	0.20	-336.81	1.74	n	n	n	n
20020506 19:15/0507 00:15	0.78	-390.00	2.46	y	n	n	n
20020507 17:30/0507 23:00	2.87	-392.40	3.49	y	n	n	n
20020514 22:45/0515 03:00	-2.42	-414.01	1.82	n	n	n	n

*Continued on next page*

Table 5 – *Continued from previous page*

Start/End	OMNI			Cluster SC3			
	$B_z$ [nT]	$V_x$ [km/s]	P $[cm^{-3}]$	$B_z$	$V_x$	$n_{CIS}$	$n_{EFW}$
20020517 07:00/0517 12:15	-0.39	-379.32	1.52	y	y	y	y
20020518 13:30/0518 19:30	0.63	-345.87	1.59	n	n	y	y
20020519 20:00/0520 03:30	4.75	-408.56	1.12	y	y	y	y
20020520 10:45/0520 20:15	0.74	-448.89	1.93	y	y	y	y
20020522 02:00/0522 08:45	-1.07	-398.12	1.63	n	y	y	y
20020527 02:15/0527 17:15	-3.11	-542.53	2.07	y	y	y	y
20020530 05:00/0530 10:30	0.03	-493.86	2.08	y	n	y	y
20020601 19:30/0602 01:00	-3.38	-342.27	4.16	y	y	y	y
20020602 21:45/0603 17:45	0.38	-435.47	1.89	y	y	y	y
20020605 10:30/0606 06:00	-0.42	-394.49	1.08	y	y	n	n
20020607 18:00/0607 22:00	-1.60	-291.85	1.80	y	y	y	y
20020608 01:15/0608 18:15	0.06	-335.39	2.74	y	n	y	y
20020610 01:30/0610 09:30	1.60	-465.52	3.00	y	y	y	y
20020610 11:00/0611 01:00	-2.27	-419.86	2.16	y	n	y	y
20020612 18:30/0613 06:15	-1.13	-351.03	1.16	y	y	y	y
20020615 07:00/0615 23:30	-1.16	-334.27	2.84	n	n	y	y
20020617 05:00/0618 03:45	0.78	-351.47	1.87	y	n	y	y
20020620 04:00/0620 11:00	0.46	-485.48	1.73	y	y	y	y
20020622 14:30/0622 18:00	-0.72	-429.02	1.93	n	n	y	y
20021201 04:15/1202 07:45	-1.09	-499.23	2.62	y	y	y	y
20021203 15:30/1204 19:30	0.34	-449.09	2.06	y	n	n	n
20021207 00:30/1207 07:45	0.80	-451.80	7.33	n	n	y	y
20021208 09:30/1209 08:00	0.60	-600.27	1.49	y	n	y	y
20021212 23:30/1213 14:30	0.10	-337.77	1.32	y	n	n	n
20021213 21:15/1214 09:30	-0.74	-361.19	2.99	y	n	y	y
20021215 12:45/1216 18:00	1.32	-479.48	1.53	y	n	n	n
20021217 16:30/1218 01:45	4.56	-393.99	2.49	y	n	y	y
20021220 01:30/1220 06:15	-1.21	-530.62	3.01	y	n	y	y

*Continued on next page*

Table 5 – *Continued from previous page*

Start/End	OMNI			Cluster SC3			
	$B_z$ [nT]	$V_x$ [km/s]	P $[cm^{-3}]$	$B_z$	$V_x$	$n_{CIS}$	$n_{EFW}$
20021223 02:15/1223 13:00	-2.32	-516.12	2.22	y	n	n	n
20021223 14:00/1223 22:30	0.89	-519.77	2.55	y	y	y	y
20021224 19:00/1225 01:45	0.88	-523.86	3.41	y	n	y	y
20021225 23:45/1226 07:15	-0.61	-414.38	2.21	y	y	n	n
20021226 23:00/1227 09:45	-1.79	-618.14	6.20	y	y	y	y
20021229 11:45/1229 17:00	-0.41	-580.12	2.39	y	n	n	n
20021230 17:45/1231 01:00	-1.01	-483.60	1.93	y	n	n	y
20021231 23:00/0101 05:15	0.60	-418.95	1.94	y	n	n	n
20030105 14:00/0105 21:00	-0.03	-414.46	1.69	y	n	n	n
20030106 23:15/0107 03:00	-1.62	-392.29	1.56	n	n	n	n
20030109 08:45/0109 16:15	1.45	-272.82	2.31	n	n	n	n
20030110 07:15/0110 15:15	-2.11	-401.03	2.72	y	n	y	y
20030111 08:15/0111 22:30	-0.20	-433.33	1.24	y	n	n	y
20030112 17:30/0113 00:15	1.53	-389.62	1.45	y	n	n	n
20030114 00:30/0114 08:30	-1.67	-388.53	2.27	y	n	n	y
20030116 10:15/0116 17:45	-1.20	-328.91	1.22	n	n	n	n
20030117 09:30/0117 13:30	-1.36	-327.09	2.55	y	y	y	y
20030118 23:30/0119 03:45	6.41	-459.46	4.82	y	y	y	y
20030119 21:00/0120 01:00	1.52	-597.95	2.38	y	n	y	y
20030121 06:30/0121 11:30	-1.77	-670.25	1.50	y	n	n	n
20030122 04:45/0122 09:30	0.11	-588.87	2.30	y	n	y	y
20030126 01:45/0126 06:30	-0.24	-713.82	2.75	y	y	y	y
20030127 08:15/0127 13:00	7.94	-509.30	0.47	y	n	y	y
20030128 12:30/0128 17:15	4.95	-443.83	4.15	y	y	y	y
20030130 19:45/0131 00:15	4.21	-510.33	2.63	y	n	y	y

Start/End	GUMICS Neutral Sheet
20020901 19:10/0901 23:54	–
20020906 14:07/0906 16:37	+
20020913 17:33/0913 20:06	+
20020918 12:47/0918 14:26	–
20020920 20:36/0921 02:13	+
20020928 02:58/0928 07:00	+
20021002 16:12/1002 23:52	–
20021014 12:34/1014 22:53	+
20021017 03:08/1017 04:11	–

845      **Table 6.** Intervals around the studied neutral sheet crossings in the tail. The Cluster SC3  
 846      crossed the neutral sheet in all cases. The 3rd column shows whether the neutral sheet is visible  
 847      in the GUMICS–4 simulations.